

# **UK-HiGEM: The New UK High Resolution Global Environment Model.**

## **Model description and basic evaluation.**

Len Shaffrey<sup>1</sup>, Ian Stevens<sup>2</sup>, Warwick Norton<sup>1</sup>, Malcolm Roberts<sup>3,4</sup>, Pier-Luigi Vidale<sup>1,3</sup>,  
James Harle<sup>7</sup>, Amna Jrrar<sup>8</sup>, Dave Stevens<sup>2</sup>, Margaret Woodage<sup>9</sup>, Marie-Estelle Demory<sup>1,3</sup>,  
John Donners<sup>1,3</sup>, Douglas Clark<sup>5</sup>, Adam Clayton<sup>3,4</sup>, Jeff Cole<sup>1</sup>, Simon Wilson<sup>1,4</sup>,  
William Connolley<sup>8</sup>, Terry Davies<sup>6</sup>, Alan Iwi<sup>10</sup>, Tim Johns<sup>4</sup>, John King<sup>8</sup>,  
Adrian New<sup>7</sup>, Julia Slingo<sup>1</sup>, Anthony Slingo<sup>9</sup>, Lois Steenman-Clark<sup>1</sup>, Gill Martin<sup>4</sup>.

February 27, 2008

<sup>1</sup> National Centre for Atmospheric Science, Department of Meteorology, University of Reading,  
UK

<sup>2</sup> School of Mathematics, University of East Anglia, Norwich, UK

<sup>3</sup> UK-Japan Climate Collaboration, Earth Simulator Centre, Yokohama, Japan

<sup>4</sup> Met Office Hadley Centre for Climate Prediction and Research, Exeter, UK

<sup>5</sup> Centre for Ecology and Hydrology, Wallingford, UK

<sup>6</sup> Met Office, Exeter, UK

<sup>7</sup> National Oceanography Centre Southampton, University of Southampton, UK

<sup>8</sup> British Antarctic Survey, Cambridge, UK

<sup>9</sup> Environmental Systems Science Centre, University of Reading, UK

<sup>10</sup> British Atmospheric Data Centre, Rutherford Appleton Laboratory, UK

**Submitted to Journal of Climate**

## Abstract

This paper describes the development and evaluation of the UK's new high resolution global coupled model, HiGEM, which is based on the latest climate configuration of the Met Office Unified Model, HadGEM1. In HiGEM, the horizontal resolution has been increased to  $1.25^\circ \times 0.83^\circ$  in longitude and latitude for the atmosphere, and  $1/3^\circ \times 1/3^\circ$  globally for the ocean. Multi-decadal integrations of HiGEM, and the lower resolution HadGEM, are used to explore the impact of resolution on the fidelity of climate simulations.

Generally SST errors are reduced in HiGEM. Cold SST errors associated with the path of the North Atlantic drift improve, and warm SST errors are reduced in upwelling stratocumulus regions where the simulation of low level cloud is better at higher resolution. The ocean model in HiGEM allows ocean eddies to be partially resolved, which dramatically improves the representation of sea surface height variability. In the Southern Ocean, most of the heat transports in HiGEM is achieved by resolved eddy motions which replaces the parametrised eddy heat transport in the lower resolution model. HiGEM is also able to more realistically simulate small-scale features in the windstress curl around islands and oceanic SST fronts, which may have implications for oceanic upwelling and ocean biology.

Higher resolution in both the atmosphere and the ocean allows coupling to occur on small spatial scales. In particular the small scale interaction recently seen in satellite imagery between the atmosphere and Tropical instability waves in the Tropical Pacific ocean is realistically captured in HiGEM. Tropical instability waves play a role in improving the simulation of the mean state of the Tropical Pacific which has important implications for climate variability. In particular all aspects of the simulation of ENSO (spatial patterns, the timescales at which ENSO occurs, and global teleconnections) are much improved in HiGEM.

# 1. Introduction

This paper is the first in a series describing the development and performance of the UK's first high resolution global environment model (HiGEM). These papers will highlight different aspects of the Earth system and the new perspectives that high resolution has brought to the simulation of the coupled system. The HiGEM project is a partnership between the Natural Environment Research Council (NERC), the UK academic community and the Met Office Hadley Centre. Its aim is to extend the latest climate configuration of the Met Office Unified Model, HadGEM1, to higher resolution in both the atmosphere and ocean. HiGEM has also formed the core of the modelling activities of the UK-Japan Climate Collaboration (UJCC) between the National Centre for Atmospheric Science, the Met Office Hadley Centre and the Earth Simulator Centre, in which UK staff are permanently based at the Earth Simulator Centre in Yokohama.

HiGEM represents a significant change in how global environment modelling is conducted in the UK; it brings together the fundamental research within NERC and the academic community with the climate prediction programme of the Met Office Hadley Centre. HiGEM has facilitated the engagement of NERC expertise in various aspects of climate system science with the development and evaluation of the UK's next generation model of the global environment. For the first time, many of the principal areas of NERC science are working together, leading to a concerted effort in state-of-the-art global environment modelling which hitherto has been somewhat fragmented. Moving towards higher resolution has enabled the gap to be narrowed between modellers and scientists specialising in particular processes and phenomena, and between models and observations of the Earth system.

The overarching drivers for the development of HiGEM are, firstly, to explore the impact of higher resolution on the fidelity of the simulations and, secondly, to understand the non-linear processes that give rise to interactions between small and large spatial scales, and between high and

low frequencies, within the climate system. Complex fluid flows in the atmosphere and oceans are a fundamental feature of the climate system. They transport energy, tracers, and momentum within and between system components; they occur over a wide range of spatial scales, and evolve over a wide range of time scales. A clear imperative is to develop models of much higher resolution, in order to simulate explicitly flows down to smaller scales, and to capture potential non-linear interactions between a wider range of spatial and temporal scales, and between different components of the climate system. Rapid increases in computer power are enabling much higher resolution to be used and HiGEM attempts to exploit those opportunities.

The current, state-of-the-art coupled climate models used in the IPCC 4th Assessment Report (IPCC 2007) have a typical resolution of  $\sim 1.5\text{-}3^\circ$  in the atmosphere and  $\sim 1^\circ$  in the ocean. In neither component are key aspects of the climate system (such as the influence of ocean eddies, orographic forcing of the atmosphere, tropical cyclones) adequately represented. Furthermore, during the 30 year history of climate modelling, the horizontal resolution has barely increased despite a substantial increase in the complexity of the models. Computing power has increased by several orders of magnitude, but that increase in power has been used almost exclusively to introduce more complex parametrisations and additional processes, to perform multi-century integrations and, more recently, to explore uncertainty through large ensembles of simulations.

Yet there is a strong case for higher resolution in all components of the coupled system. For the atmosphere, high resolution simulations have already demonstrated significant improvements in the representation of storm track processes and of the detailed precipitation distribution over Europe where orographic effects are important (Pope and Stratton 2002, Jung *et al.* 2006). For the ocean, there is good evidence that eddy permitting models provide a much better representation of the wind-driven circulation and western boundary currents (Semtner and Chervin, 1988; Bryan and Holland, 1989; FRAM Group 1991; Semtner and Chervin, 1992). The early eddy permitting

models also captured, for the first time, the geographical distribution of mesoscale eddy variability observed by satellite altimeters. Since the equatorial Rossby radius for ocean waves is of the order of 100-250km (e.g. Gill 1982), it is clear that higher resolution will also give a more accurate simulation of equatorial waves, which are a key part of El Nino. However, there are still deficiencies at mid to high latitudes where the Rossby deformation radius remains unresolved indicating a need for even higher resolution (Smith *et al.* 2000).

At the land surface, strong variations in properties such as topographic height, vegetation cover, soil properties, soil moisture and snow cover, occurs at all length scales. These combine non-linearly to produce large variations in surface fluxes of heat, moisture, momentum and carbon dioxide. As a result, the accurate modelling of surface processes in GCMs is strongly constrained by horizontal resolution. Numerous studies have illustrated that land surface feedbacks can affect the atmosphere at scales from the local up to the global (e.g. Taylor *et al.* 2007). Explicitly resolving finer scale surface features should lead to improvements in the simulation of climate over continental regions.

Sea ice is highly inhomogeneous, with much of the exchange of heat between ocean and atmosphere taking place over small areas of open water (leads and polynyas) within the ice cover. These exchanges of heat determine the overall growth of the winter sea ice and the consequent modification of ocean water masses through brine rejection. Correct parametrisation of these energy exchanges is essential for realistic climate simulations and requires high resolution atmospheric and oceanic fields in order to calculate the fraction of open water and its distribution within a grid cell correctly. The rheology of sea ice is also highly nonlinear. Accurate simulation of ice-ocean interactions thus requires a high spatial resolution (Holland 2001).

High resolution simulations of the climate system have generally been run in uncoupled mode and often only at a regional scale where the simulation may be compromised by errors in the

boundary forcing. The impact of details in the structures, for example the tightness of the Gulf Stream, on the evolution of the global coupled system has yet to be explored properly, although it may be substantial. For example, results from a coupled model have shown a dramatic improvement in the mean tropical climate and the simulation of El Nino when the atmosphere is run at a resolution commensurate with that of the ocean (Guilyardi *et al.* 2004). Furthermore, analyses of near-surface wind speed and direction over the global ocean from the QuikSCAT satellite radar scatterometer (Chelton *et al.* 2004) have shown persistent small-scale features indicative of air-sea interaction over sea-surface temperature fronts, such as the Gulf Stream, and the influences of islands and coastal mountains. Similarly, results from a high resolution version of the coupled MIROC3.2 climate model (K-1 Model Developers 2004) shows that resolving small scale islands and orographic features, such as the Hawaiian Islands, can have far-reaching effects on the atmosphere and ocean (Sakamoto *et al.* 2004)

This paper describes the development of HiGEM, and presents a basic evaluation of its performance from a multi-decadal integration for the current climate. Further papers will cover in more detail aspects such as weather, ocean variability and modes of climate variability (Harle *et al.* 2008; Roberts *et al.* 2008a,b; Shaffrey *et al.* 2008; Stevens *et al.* 2008). Section 2 contains a description of HiGEM including the changes made from HadGEM1, the production of the high resolution boundary conditions and the optimisation of the code. Using results from a multi-decadal simulation for the current climate, the performance of the full system and of each component of the model is described in Section 3 with a particular emphasis on the impact of high resolution on the simulation. Section 4 highlights specific coupled ocean-atmosphere interactions that are facilitated by high resolution in both the atmosphere and ocean combined. The paper concludes with some discussion and overall conclusions concerning model performance.

## 2. Model Description

HiGEM is based on the latest climate configuration of the Met Office Unified Model, HadGEM1 (Johns *et al.* 2006, Martin *et al.* 2006; Ringer *et al.* 2006), which has formed a major contribution to the IPCC 4th Assessment Report (IPCC 2007). The horizontal resolution of HadGEM1 is  $1.875^\circ \times 1.25^\circ$  in longitude and latitude (N96) in the atmosphere, and  $1^\circ \times 1^\circ$  (increasing to  $1/3^\circ$  meridionally near the equator) in the ocean.

In HiGEM, the horizontal resolution has been increased to  $1.25^\circ \times 0.83^\circ$  (N144) in longitude and latitude for the atmosphere, and  $1/3^\circ \times 1/3^\circ$  globally for the ocean and sea ice. Experience in numerical weather prediction suggests that at N144 weather systems, the building blocks of climate, are more realistically represented. Similarly, experience with high resolution ocean models suggests that at  $1/3^\circ$  ocean resolution, small-scale eddies are represented, steep gradients such as in western boundary currents are better resolved, and the ocean can be made much less diffusive. HiGEM has higher resolution in both components than has hitherto been used in the UK for extended simulations of the coupled global environment.

In the development of HiGEM, a number of versions of the model were produced. In this paper we describe HiGEM1.2 and document the changes required to produce this model from HadGEM1. An earlier version of HiGEM, HiGEM1.1 was also extensively tested and a centennial simulation was run on the Earth Simulator. This integration will be described in greater detail in Roberts *et al.* (2008a).

The move to higher resolution has necessitated some changes to the model, particularly in the ocean. Furthermore since the submission to the IPCC 4th Assessment Report, various improvements have been implemented in HadGEM1 to form the latest version HadGEM2-AO. Some of these improvements have been included in the HiGEM code.

## 2.1 Atmosphere Component

The atmosphere component of HiGEM1.2 is very similar to the HadGEM1 model (see Martin *et al.* 2006). It has a non-hydrostatic dynamical core (Davies *et al.* 2005), with semi-Lagrangian transport. Discretisation is on a Arakawa C grid. Parametrisations in HadGEM1 are substantially improved, e.g. new boundary layer and convection schemes, compared to the earlier Met Office Hadley Centre HadCM3 model (Gordon *et al.* 2000). HadGEM1 includes an interactive aerosol scheme, driven by surface and elevated emissions. Both HadGEM1 and HiGEM1.2 have 38 levels in the vertical.

With the increased resolution of HiGEM1.2 the timestep was reduced from 30 minutes (HadGEM1 value) to 20 minutes. The magnitude of polar filtering in the advection scheme was also reduced. In HadGEM1 a targeted diffusion scheme was implemented to prevent grid points storms. The vertical velocity threshold at which the targeted moisture diffusion is triggered was increased from  $0.1\text{ms}^{-1}$  in HadGEM1 to  $0.4\text{ms}^{-1}$  in HiGEM1.2.

Two improvements in HadGEM2-AO were also found to have a beneficial impact on the simulation in HiGEM1.2 and so were included. These included reducing the snow-free sea-ice albedo from 0.61 to 0.57 and changing the treatment of runoff over frozen soil. In HadGEM1 it was assumed that none of the runoff penetrated into frozen soil. When this assumption was relaxed there was marked improvement in the seasonal cycle of soil moisture and land temperatures.

HiGEM1.2 includes the total ocean current in the calculation of surface wind stress. This produces improvements in the simulation of sea surface temperatures in the tropical east Pacific compared to HadGEM1 where the ocean currents were not included. The coupling frequency is unchanged from HadGEM1, i.e. that ocean and atmosphere are coupled once per day.

## 2.2 Ocean component

The ocean component follows that used in the ocean component of HadGEM1 (Johns *et al.*, 2006), but with increased horizontal resolution and improvements to some of the model physics. The latitude-longitude grid has a singularity at the North Pole which is treated as a land point. Convergence of the meridians towards the North Pole on the spherical grid requires the tracers and baroclinic velocities to be Fourier filtered northwards of 80°N to maintain stability. No filtering is necessary in the southern hemisphere.

The ocean model has 40 unevenly spaced levels in the vertical with enhanced resolution near the surface to better resolve the mixed layer and atmosphere-ocean interaction processes. The level thicknesses are derived from an analytic expression to give near 10m resolution close to the surface, increasing smoothly to near 300m at depth. The use of an analytic function to derive the model levels results in 2nd order accurate vertical differencing (Marti *et al.*, 1992). The maximum ocean depth is 5500m.

The external mode is solved with a linear implicit free surface scheme (Dukowicz and Smith, 1994). To prevent the free surface height in marginal seas changing too far from the mean sea level an adjustment is performed after each timestep to maintain the average global free surface height. This has no impact on the dynamics as it is only gradients of free surface height which are important for a linear free surface.

Lateral mixing of tracers uses the isopycnal formulation of Griffies *et al.* (1998) with a constant isopycnal diffusivity. The Gent and McWilliams (1990) (GM) adiabatic mixing scheme which was used in the lower resolution HadGEM1 is not used in HiGEM1.2. Tests showed that its inclusion created low eddy variability, erosion of fronts and the higher horizontal resolution of HiGEM1.2 means that eddies are, at least partially, represented. The adiabatic biharmonic scheme of Roberts and Marshall (1998) (biharmonic GM) is used to reduce noise in tracer fields, particularly at high

latitudes. To represent enhanced mixing at the ocean surface, tracers at levels 1 and 2 are mixed horizontally using a biharmonic scheme. All the biharmonic mixing schemes use constant coefficients scaled by  $\cos^3(\text{latitude})$  for numerical reasons to deal with the convergence of meridians approaching the North Pole.

The vertical mixing of tracers uses a hybrid scheme. The diffusivity at all depths is set using the Richardson number parametrisation subject to a minimum, depth dependent background diffusivity. A bulk mixed layer scheme is used to determine the tracer values in the mixed layer. The vertical mixing of momentum also uses an hybrid scheme with a similar Richardson number parametrisation to that used for vertical tracer mixing, but subject to a constant minimum background diffusivity. The mixing of momentum in the mixed layer is represented by assuming the diffusion coefficient is a quadratic function of depth. For both momentum and tracers, the diffusivity is enhanced immediately below the mixed layer base to reduce the large gradients which can occur in this region.

Tracers are advected using a pseudo fourth-order scheme (Pacanowski and Griffies, 1998) except at the bottommost level which uses an upwind scheme to reduce tracer extrema. Momentum advection uses a second order centred difference scheme. Bottom friction is implemented using a quadratic semi-implicit scheme.

The equation of state (EOS) used in HiGEM1.2 is that given in McDougall *et al.* (2003). The UNESCO EOS (Gill, 1982) was updated by Feistel and Hagen (1995) by including more recent data. However, this gives density as a function of pressure, salinity and in-situ temperature. McDougall *et al.* (2003) derived a 25 term fit in terms of pressure, salinity and potential temperature, more convenient as the model uses potential temperature. A reference density (required by the Boussinesq approximation) of  $\rho_0 = 1.035 \text{ g cm}^{-3}$  is used. Convection is parametrised using the full convection algorithm of Rahmstorf (1993). Further details of the ocean physics parametrisa-

tions are given in the companion paper by Stevens *et al.* (2008).

## 2.3 Sea Ice component

The configuration of the sea ice component in HiGEM1.2 follows closely that used in HadGEM1, with the exception of changes to the values of some parameters and the introduction of a sub-time stepping scheme for the ice dynamics. The main features are summarised below and further details can be found in McLaren *et al.* (2006). It contains elements of the CICE elasto-viscous-plastic model (Hunke and Lipscomb 2004).

Rather than existing as a separate sub-model the major part of the sea ice component resides within the ocean model with a small part in the atmosphere model. The ocean part solves for the dynamics, mechanical redistribution (ridging) and some of the thermodynamics. The atmosphere part calculates the atmosphere-ice fluxes and the ice surface temperature using the atmosphere timestep to allow representation of the diurnal cycle. These fields are then averaged and communicated to the ocean model on a coupling timestep.

The ice pack is modelled as a five category ice thickness distribution which evolves through advection, ridging and thermodynamic growth or melt. The ice velocities are calculated by solving the ice momentum equation using the Elastic Viscous Plastic (EVP) model of Hunke and Dukowicz (1997). The rate of change of ice momentum is a balance between ice-air drag, ice-ocean drag, Coriolis force and internal ice stresses. The stresses are calculated from a constitutive equation which relates the ice stresses to the strain rates using an EVP rheology. The ice velocities are used to advect each ice category and the open water category using an upwind scheme. Following advection, the ridging scheme (Hunke and Lipscomb, 2004) converts thin ice into thick ice and creates open water. This ensures that in regions of convergent flow the ice area cannot exceed the grid cell area. The thermodynamic growth/melt is represented using the zero layer model of

Semtner (1976), applied to each category. The zero layer model implies that there is no heat storage within the ice. After the thermodynamic model has calculated the thickness growth rates the linear remapping scheme of Lipscomb (2001) is used to calculate the transfer of ice between categories.

The ice model parameters are the same as those used in HadGEM1 with the exception of those related to the EVP subcycle timestep. The EVP model introduces an elastic component to the Viscous Plastic (VP) rheology as a means to increase the efficiency of the ice stress calculation. The EVP calculation is subcycled with a timestep which is  $O(100)$  times smaller than the ocean timestep. In the limit of a very small subcycle step the EVP solution converges to the VP solution. Taking many subcycle steps is computationally expensive but if insufficient steps are taken elastic waves can remain in the solution which leads to noisy ice velocities. The ocean timestep in HadGEM1 is 1 hour and the EVP subcycle step is 30 s. HiGEM1.2 has an ocean timestep of 20 mins and an EVP subcycle step of 10 s.

The presence of a land point at the North Pole on the ocean grid means that no thermodynamic processes can affect the ice concentration at this point. However, sea ice does exist at this point and its evolution is calculated by a scheme that advects ice over the pole using ice velocities from the row immediately to the south.

In some early runs there were problems with stability of the ice model close to the north polar island. The ice velocities at the northernmost ocean row became large enough to violate the CFL stability criterion due to the convergence of meridians. The resulting noisy ice concentration field meant that the ridging process was unable to converge in a reasonable number of steps and the model crashed with negative ice concentrations. In the ocean the stability problems are solved by Fourier filtering the velocity and tracer fields. Filtering cannot be performed on the ice velocities because it changes the mask of icy/non-icy grid cells. A possible solution would be to reduce the ocean timestep which is undesirable because it reduces the speed of the whole model. An

alternative solution which has been implemented is to sub-timestep the ice dynamics and ridging calculations. The calculation of the ice velocities, the advection of the individual categories and the ridging calculation is performed twice, with a timestep of half the ocean timestep followed by the thermodynamic part of the calculation over a whole ocean timestep.

## 2.4 Boundary Conditions

### (a) Bathymetry

The bottom topography is derived from two datasets, the  $1/12^\circ$  GEBCO Digital Atlas (IOC *et al.*, 2003) and the  $1/30^\circ$  dataset of Smith and Sandwell (1997). Both datasets are interpolated to the model grid by taking the median of all depths within each  $1/3^\circ \times 1/3^\circ$  grid cell for those cells where more than 62.5 % of the points are sea points. This was found to give the best representation of coastlines. The resulting depth fields were not smoothed. In some regions, particularly the deep ocean basins there are significant differences between the two datasets. In these regions the model depth was taken as the mean of the GEBCO and Smith and Sandwell (1997) values. The model depths were converted to model levels, and isolated bays (grid cells unaffected by advection) and single grid cell holes were filled. The topography was then adjusted in the regions of key sills and narrow pathways using data from Thompson (1995).

The land-sea mask is based on the GEBCO dataset with some adjustment of the coastline to give as accurate a representation as possible, commensurate with the  $1/3^\circ$  degree horizontal resolution. The connection between the Mediterranean Sea and the Atlantic Ocean at the Strait of Gibraltar is unresolved by the model grid, which requires a width of two tracer cells, or approximately 74 km, to allow an advective transport. The Strait of Gibraltar is 12 km wide, so rather than modifying the topography to widen the Strait, the choice was made to close the Strait with a land barrier. The Mediterranean Outflow strongly affects water mass properties in the Atlantic Ocean

so the exchange of tracers is parametrised as a volume flux of +0.5 Sv (Atlantic to Mediterranean) in the upper ocean and a return volume flux of equal magnitude at depth. The entrances to the Red Sea and Persian Gulf are sufficiently well resolved to be open to the Indian Ocean. The Black Sea, Caspian Sea and Great Lakes are represented but are not connected to other ocean basins.

### **(b) Land surface conditions**

The model requires input datasets (ancillary files) to provide information about surface boundary conditions, such as orography, and other climatological fields, such as vegetation cover, which the model does not predict. The starting point in creating the ancillary files is deriving the land fraction from the land/sea mask of the ocean model. The coastal tiling scheme in the model enables a more accurate representation of fluxes at land-sea boundaries by combining ocean and land surface fluxes in proportion to the fraction of land within the gridbox.

The orography has been derived from the 1' GLOBE dataset, which provides an accurate representation of the mountains and their sub-gridscale characteristics. The orography is smoothed with a Raymond filter to remove grid-scale and sub-grid scale features that are poorly represented in the model (Webster *et al.* 2003).

The land surface scheme of HadGEM1 uses fractional tiling to represent sub-gridscale surface heterogeneity. Nine land surface types are used, which include five vegetation types (C3 and C4 grasses, shrub, needleleaf and broadleaf trees), bare soil, urban, permanent ice and open water. Seasonally varying vegetation fractions for the five vegetation types were derived from the IGBP dataset (Loveland *et al.* 2000). A new specification for the soil albedo based on the analysis of MODIS data has been implemented over the Sahara (Holdcroft *et al.* 2008). Previously the distribution of soil albedo over the Sahara was too uniform and had unrealistically high values.

### **(c) Aerosol emissions and greenhouse gases**

The interactive aerosol scheme in HiGEM1.2 requires emissions data and oxidant fields to

drive the sulphur, black carbon and biomass burning modelling. The raw datasets on which these are based are the same as for HadGEM1 (Martin *et al.* 2006), but interpolated to the higher horizontal resolution required for HiGEM1.2 (the vertical resolution is the same). For the sulphur cycle, seasonal anthropogenic sulphur dioxide emissions representing present-day values are from Smith *et al.* (2004). Natural emissions of dimethyl sulphide (DMS) on land are from Spiro *et al.* (1992), and monthly mean sea water concentrations of DMS are from Kettle *et al.* (1999). Annual mean volcanic sulphur emissions representing constantly-emitting sources are from Andres and Kasgnoc (1998). Monthly mean 3-dimensional fields of oxidants (OH, H<sub>2</sub>O<sub>2</sub> and HO<sub>2</sub>) for the sulphur cycle are taken from the off-line STOCHEM model (Collins *et al.* 1997). Annual mean black carbon (soot) and monthly mean biomass burning aerosol emissions are taken from Nozawa (2003, personal communication to Hadley Centre).

The model is forced with fixed present-day concentrations of trace greenhouse gases (the mass mixing ratios of CO<sub>2</sub>, CH<sub>4</sub>, N<sub>2</sub>O are 5.241e-04, 9.139e-07 and 4.665e-07 respectively). Ozone is a seasonally varying two dimensional field (latitude-height) derived from the SPARC climatology for 1990 (Randel and Wu, 1999).

## 2.5 Model optimisation

HiGEM1.2 is computationally very demanding and good optimisation of the code was considered essential to ensure efficient use of computing resources and to achieve a wallclock time that is fast enough to enable a multi-decadal simulation within a few months. HiGEM1.2 has been implemented on the UK Research Council's HPCx system (IBM p5-575 cluster) and on the Earth Simulator.

The target performance of HiGEM1.2 was set at a minimum of 1 year of simulation per day. The unoptimised code was found to spend nearly 60% of the time in inter-process communication,

most of which was in the conjugate gradient solver routine in the ocean code. Furthermore the sea ice code was found to be poorly load balanced. Implementing a faster global sum in the conjugate gradient solver and better load balancing in the sea ice resulted in a 62% speed-up of the code. With these improvements HiGEM1.2 can achieve its target performance of 1 year of model simulation per day on 256 processors on the HPCx system.

## 2.6 Model initialisation and integrations

The atmosphere initial conditions were created from a September ECMWF analysis field, with land surface conditions set to values from the ancillary files. The ocean initial conditions were created using potential temperatures and salinities interpolated from the 1/4° World Ocean Atlas 2001 (Conkright *et al.* 2002), with initial ocean currents at rest. The sea ice fields were interpolated from September HadGEM1 model fields.

To demonstrate the impact of increased resolution an equivalent lower resolution control, HadGEM1.2, has also been developed. HadGEM1.2 is very similar to HadGEM1 (Johns *et al.*, 2006) but implements most of the changes to the parametrisations that are in HiGEM1.2. HadGEM1.2 has the same horizontal and vertical grids in the atmosphere and ocean as HadGEM1 and also uses identical bathymetry and orography.

Differences in the ocean code between HadGEM1.2 and HiGEM1.2 mainly result from the different horizontal resolution. In HiGEM1.2 the entrances to the Red Sea and Persian Gulf are resolved by the model grid, but the coarser resolution of HadGEM1.2 requires that these are parametrised. The horizontal mixing coefficients are larger than in HiGEM1.2, commensurate with the coarser grid, and the timestep is increased to 1 hour. HadGEM1.2 uses the Gent and McWilliams (1990) adiabatic mixing scheme with the coefficients determined from the Visbeck *et al.* (1997) scheme. Horizontal viscosity in HadGEM1 was a combination of Laplacian with

constant coefficient and biharmonic with coefficient scaled by  $\cos^3(\text{latitude})$ . Investigations at the Met Office Hadley Centre found improvements to the equatorial circulation by changing the constant Laplacian viscosity to an anisotropic scheme. This is the formulation used in HadGEM1.2. The Laplacian viscosity has a zonal coefficient given by  $K_x = 750 (1 - \cos(\text{latitude})) \text{ m}^2\text{s}^{-1}$  and a meridional value,  $K_y = K_x(\Delta x/\Delta y)$  where  $\Delta x$  and  $\Delta y$  are the zonal and meridional grid spacings. The only differences in the sea ice model are that HadGEM1.2 has an EVP subcycle timestep of 30s and does not use the dynamics subtimestepping scheme.

Both the HiGEM1.2 and HadGEM1.2 were run for 70 years from the same initial conditions. A slightly earlier version of HiGEM, HiGEM1.1, has also been run for 130 years on the Earth Simulator in Japan. Many aspects of the model's performance are similar to those of HiGEM1.2 and some limited results will be used to demonstrate the level of skill in capturing El Nino when more than 70 years of simulation are required to assess its temporal characteristics. More details on this simulations can be found in Roberts *et al.* (2008a,b)

### **3. Evaluation of model performance**

The evaluation of the high resolution model simulations has involved the wide range of NERC expertise related to the various components of the climate system, and used recent developments in earth observation for several components of the system. In this paper the focus will be on the mean state of the global climate system and how resolution in the atmosphere and/or ocean improves the overall performance of the model. One of the major results from HiGEM1.2 has been the representation of fine scale air-sea coupled processes, especially in the Tropical Pacific, as well as significant improvements in the simulation of El Nino and its global effects. A basic description of these achievements will be provided in Section 4, and more detailed aspects of these

phenomena, and of weather and ocean variability in HiGEM will be presented in related papers (Harle *et al.* 2008; Roberts *et al.* 2008a,b; Shaffrey *et al.* 2008; Stevens *et al.* 2008).

### 3.1 Overall energy balance

Table 1 compares the annual, global mean energy balance of the HiGEM1.2 and HadGEM1.2 simulations with observational estimates. The models show similar characteristics compared with the observations. The net radiation in both cases is close to balance, but this is achieved by reflecting too little solar radiation back to space and emitting too much thermal radiation. These characteristics are enhanced in HiGEM1.2, which has slightly less cloud and sea ice than the HadGEM1.2, more solar absorption at the surface and consequently higher surface temperatures. It was decided not to attempt to re-tune HiGEM1.2 to bring the net radiation into balance, because the radiation imbalance is not large and the initial emphasis is to examine the impact of higher resolution on atmospheric and oceanic processes, rather than to perform long-range climate predictions.

The differences between HiGEM1.2 and HadGEM1.2 also influence the evolution of the radiation balance and surface temperatures, as the models spin-up to equilibrium during the integrations (Figure 1). Initially both models cool in accordance with the negative net top-of-atmosphere (TOA) radiation. The net outgoing longwave radiation (OLR) falls and the net TOA radiation rapidly adjusts to being slightly positive in HiGEM1.2 and to near zero in HadGEM1.2. As a result of the positive net TOA flux, HiGEM1.2 gradually warms to reach an equilibrium global mean surface temperature close to the initial condition, whereas HadGEM1.2 remains cold.

The evolution of the sea ice has an impact on the longer timescale evolution of the global radiation balance. Over the first few decades there is a reduction in sea ice in HiGEM1.2 (Figure 1f) mostly around the Antarctic (see section 3.6). After year 30 some Antarctic sea ice reforms, which leads to a reduction in net surface solar and a small reduction in the net TOA. It is also worth

noting that in both models the net TOA has a small but positive value into the climate system. As shown by Johns *et al.* (2006) in HadGEM1 this is stored as heat in the ocean subsurface. A similar evolution of subsurface ocean temperatures occurs in HiGEM1.2 and will be discussed in greater detail in Stevens *et al.* (2008).

Figure 2 shows the geographical distributions of the reflected solar, outgoing thermal and net radiation at the top of the atmosphere from HiGEM1.2, and the differences from the HadGEM1.2 control. The fields are averaged over years 21 to 70. The choice of averaging period was based on the time taken for the initial spin-up of the TOA to become small. Unless otherwise stated, subsequent figures showing the means of various model quantities are also based on 21 to 70 year averages.

The tendency for lower cloud amounts in HiGEM1.2 is apparent in the generally negative values in the reflected solar differences. Martin *et al.* (2006) show that the simulation of subtropical marine stratocumulus in the atmosphere-only version of HadGEM1 is considerably better than that in the previous model, HadAM3. Figure 2 shows that this is also the case in the control integration of HiGEM1.2: note the maxima in the reflected solar off the west coasts of the continents, particularly off North and South America. The difference plot shows positive values close to these coasts and negative values further West, indicating that the cloud in HiGEM1.2 is concentrated closer to the land than in HadGEM1.2, in better agreement with the ERBE observations shown by Martin *et al.* (2006). Although the changes appear to be small, it is known that the simulation of sea surface temperatures in this region and in the eastern tropical Pacific, in general, are very sensitive to the cloud distribution (Ma *et al.* 1996).

There are also both positive and negative differences in the reflected solar and outgoing thermal fields over the tropical Indian and Pacific oceans, due to systematic shifts in cloud cover. The large differences in both fields close to Antarctica are not due to cloud but to the smaller amounts of sea

ice in HiGEM1.2. The effects of both the cloud and sea ice changes are readily apparent in the net flux differences, although the changes in the tropics disappear because of the tendency for the solar and thermal effects of clouds on top of atmosphere fluxes to cancel over regions of deep tropical convection. This cancellation was first observed by ERBE and the fact that it occurs in the model is a further positive aspect of the simulations.

### **3.2 Surface climate**

As already noted, globally HiGEM1.2 has slightly less cloud than HadGEM1.2 (see Table 2), which results in warmer surface temperatures. This can be seen in more detail in Figure 3, which shows the annual mean sea surface temperature (SST) errors versus the WOA 2001 (Conkright *et al.* 2002) climatology from both models and the difference between them. The warming of HiGEM1.2 relative to HadGEM1.2 means that the cold biases in the Tropical and Subtropical Pacific, Atlantic and Indian Oceans in HadGEM1.2 are somewhat alleviated. In common with most coupled models (e.g. IPCC 2007), there are warm biases in the upwelling zones off the Peruvian, Namibian and Californian coasts, where the subtropical stratocumulus cloud decks are prevalent, but are poorly captured by models. The warm bias is slightly weaker in HiGEM1.2 in association with increased cloud cover and better resolved coastal upwelling (Roberts *et al.* 2008c).

Overall the east-west temperature gradient across the equatorial Pacific is better represented in HiGEM1.2, as is evident from the slight warming in the west and cooling in the east relative to HadGEM1.2 (Figure 3c). This has important implications for the mean state of the coupled system; the excessively strong trade winds in HadGEM1.2 are reduced and the thermocline is less steeply tilted. Both aspects have proved crucial for producing a significant improvement in El Nino and its global impacts (see Section 4). The mean state of the tropical Pacific in HiGEM is described in

more detail in Roberts *et al.* (2008a) and its importance for the simulation of El Nino in Roberts *et al.* (2008b).

The higher resolution ocean model in HiGEM1.2 also allows a tightening of the SST gradients in the Gulf Stream, some improvements in the orientation of the Gulf Stream and North Atlantic Drift, and consequently to a reduction in the temperature errors in the North Atlantic. This has a large impact on the wintertime cyclogenesis over the North Atlantic, discussed in more detail in Shaffrey *et al.* (2008). Another difference between the models is the marked Southern Ocean warm bias in HiGEM1.2, which is associated with a reduction in Antarctic sea ice (see section 3.6). This bias reduces in magnitude in the last few decades of the integration as the Antarctic sea ice partially reforms.

The annual mean Sea Surface Salinity (SSS) errors versus Levitus are shown for both HiGEM1.2 and HadGEM1.2 in Figure 3. The SSS errors in HiGEM1.2 are generally smaller than those in HadGEM1.2 which tends to be too fresh. However the saline error in the Tropical Pacific, which occurs in both models, is larger in HiGEM1.2. Both HadGEM1.2 and HiGEM1.2 are too saline in the Arabian Sea and the Bay of Bengal, associated with the lack of precipitation in the summer Indian monsoon in both HadGEM1.2 and HiGEM1.2 (see Figure 6), a persistent feature of this family of Met Office Hadley Centre models (see Martin *et al.* 2006). The differences in SSS between the two models can be attributed in part to a slightly higher excess of evaporation over precipitation over the oceans in HiGEM1.2 (see Table 1), but may also be due to differences in upper ocean mixing described in more detail in Stevens *et al.* (2008).

The annual mean 1.5m temperature errors over land for both HiGEM1.2 and HadGEM1.2 versus the CRU land temperature climatology for 1961 - 1990 (New *et al.* 2002) are shown in figure 4. Similar to the global mean surface temperatures and SSTs, the land surface of HiGEM1.2 is slightly warmer than HadGEM1.2, although both models are generally colder than the CRU

dataset, especially over the Sahara, Saudi Arabia and Central Asia and at high latitudes over North America. The increased land surface temperatures in HiGEM1.2 improve some of the cold biases in HadGEM1.2, particularly over Australia, central and southern Africa and South America. In a few places HiGEM1.2 is now warmer than the CRU dataset, for example over the Indian subcontinent and the Guiana Highlands in South America, which may be associated with soil drying due to deficient rainfall (Figure 6). Both models have deficient rainfall in these regions, so the temperature biases suggest that HiGEM1.2 has an overall more realistic land surface energy budget than HadGEM1.2. It is also worth noting that the cold temperature biases over the Sahara, West Africa and Saudi Arabia are now substantially less than those in the original version of HadGEM1 used in IPCC AR4, primarily as a result of including the MODIS derived soil albedos instead of the constant values used in HadGEM1.

The annual mean precipitation distributions from HiGEM1.2 and from a 10 year climatology of merged TRMM satellite and rain gauge observations (Huffman *et al.* 2007) are shown in Figure 5. The improved representation of orographic forcing in HiGEM1.2 is evident in a comparison of the observed and modelled distributions of precipitation. The spatial pattern of precipitation in the vicinity of mountain ranges such as the foothills of the Himalaya, the Ethiopian Highlands or those on the islands of the Maritime Continent are well captured in HiGEM1.2. Similarly spatial patterns of precipitation are well captured over strong SST fronts such as the Gulf Stream and along coastlines facing the prevailing winds, for example the Eastern coastline of the Black Sea or the South Island of New Zealand.

However it is clear in Figure 5 that there are large scale errors in the modelled distribution of precipitation. This can be seen more clearly in figure 6 which shows the annual mean errors for HiGEM1.2 and HadGEM1.2 versus the CMAP climatology (Xie and Arkin 1997). The global pattern of precipitation errors is generally unchanged with resolution, although the magnitude of

the errors are slightly reduced in HiGEM1.2. There is a marked reduction in precipitation errors along the Tropical Pacific ITCZ and over the Tropical Indian Oceans, consistent with the pattern of SST errors shown in Figure 3. Although the east-west SST gradient is improved in HiGEM1.2, it is still sufficiently in error that rainfall remains enhanced over the Maritime Continent. A recent study by Strachan (2007) has demonstrated that the pattern of errors in the Indian Ocean can be linked dynamically to those over the Maritime Continent, so it is not surprising that the Tropical error pattern is largely unchanged in HiGEM1.2.

One of the most serious and persistent errors in all versions of HadGEM is the lack of summer monsoon rainfall over India. This is clearly evident in the annual mean error patterns and is not alleviated by the higher resolution and improved representation of orography in HiGEM1.2. As will be shown later, the low level monsoon flow is, if anything, slightly too strong. Analysis of both integrations suggests that the lack of rainfall is not due to inadequate moisture supply, but to anomalous advection of dry air aloft which acts to cap the convection. The lack of monsoon rainfall leads to strong summertime drying of the Indian land surface, which creates a further feedback on the monsoon precipitation. The impact of precipitation errors on soil moisture, and other details of the land surface processes in HiGEM1.2, will be discussed further in Clark et al (2008).

Outside the tropics, however, HiGEM1.2 does show some improvements, especially over the North Atlantic where the improved structure and orientation of the Gulf Stream and North Atlantic Drift in HiGEM1.2 has led to changes in the storm track and the rain bearing systems.

### **3.3 Atmosphere**

Even though the increase in the horizontal resolution of HiGEM1.2 is less marked for the atmospheric component than it is for the ocean, it is nonetheless important to characterise and understand the changes in the atmosphere due to an increase in the resolution. A number of previous

studies have investigated the sensitivity of different aspects of atmospheric models to horizontal resolution (e.g. Pope and Stratton 2002) but none of these studies have considered this in the context of a fully coupled ocean-atmosphere system where the SSTs can respond to the atmospheric scales of motion.

The differences between the atmospheric circulation in HadGEM1.2 and HiGEM1.2 are most pronounced during boreal winter. The differences at the surface can be seen in Figure 7 which shows the DJF mean sea level pressure errors against ERA-40 for HiGEM1.2 and HadGEM1.2. The mean sea level pressure errors in HiGEM1.2 have some similarities with those in HadGEM1.2 but are mostly smaller in magnitude, and some major errors in HadGEM1.2, and indeed in earlier versions of HadGEM1 (Johns *et al.* 2006) are largely eliminated in HiGEM1.2. The Aleutian Low, which is very weak in HadGEM1.2, is better represented in HiGEM1.2, while the Icelandic Low, which is too strong in HadGEM1.2, is largely corrected in HiGEM1.2. However, the high pressure error over the Azores remains, implying that the surface westerlies over the North Atlantic are still slightly too strong in HiGEM1.2. There are also some improvements in the mean sea level pressure errors over the Southern Oceans in HiGEM1.2, particularly to the east of the Drake passage.

The improvements in the mean sea level pressure errors in HiGEM1.2, especially over the North Pacific, can be interpreted in terms of a Rossby wave train emanating from the tropical Pacific. Figure 9a shows the difference in 500hPa geopotential height between the two models, which clearly demonstrates a PNA-type pattern with a succession of anticyclonic and cyclonic anomalies extending as far as the North Atlantic. The substantial improvement in the representation of the Aleutian Low in HiGEM1.2 is clearly linked to this pattern.

There is good evidence to link this pattern of geopotential height anomalies with significant changes in tropical precipitation between the two models in boreal winter. Figure 9b shows the difference in DJF precipitation and 200hPa divergence for HiGEM1.2 minus HadGEM1.2. The

most noticeable changes in precipitation are over the north-west Tropical Pacific where there is a strong increase in precipitation over the seas surrounding the Philippines. Associated with the differences in tropical precipitation are changes in the upper level divergent flow. Regions where the changes in the upper level divergent flow impinge upon the gradient of absolute vorticity (e.g. near the flanks of the subtropical jet) will act as Rossby wave source regions (Sardeshmukh and Hoskins 1988). The region of anomalous upper level divergence around the Philippines is one such Rossby wave source region, and the cyclonic response over the North Pacific is reminiscent of the Rossby wave response generated by anomalous heating in the Tropics (Hoskins and Karoly 1981). It seems reasonable to argue therefore that the improvements in the northern hemisphere extratropical circulation during boreal winter in HiGEM1.2 can be attributed to improvements in the SST patterns and hence precipitation distributions over the Pacific warm pool.

On the other hand, the reduction of precipitation in the Tropical Pacific ITCZ evident in Figure 6, appears to be associated with a weakening of the North Pacific trade winds, which in turn may be related to a slight weakening of the North Pacific High in HiGEM1.2. This suggests that the reduction in precipitation in the Tropical Pacific ITCZ is a response to changes in the circulation induced by the increase in precipitation around the Philippines. The improvement in the representation of the Icelandic Low in HiGEM1.2 might also be interpreted as part of the Rossby Wave response emitted from the Tropical Pacific. However there are also significant anomalies of precipitation in the Tropical Atlantic that might force remote response over the North Atlantic (e.g. Sutton *et al.* 2001) and also changes in the North Atlantic SST which have an impact locally on the atmosphere (e.g. Kushnir *et al.* 2002).

The improvement in boreal wintertime circulation in HiGEM1.2 is further demonstrated in the 200hPa zonal wind shown in Figure 8. The location of the subtropical jet over the North Pacific is substantially improved, as expected from the stationary Rossby wave pattern shown in Figure 9.

The strength and orientation of the subtropical jet is also improved over the North Atlantic.

In terms of the boreal summer climate, the impact of higher resolution is less evident. Figure 10 shows the JJA errors in the 850hPa wind field in HiGEM1.2 and HadGEM1.2 versus ERA-40. Both models have an overly intense South Asian Monsoon flow, despite the lack of rainfall over the Indian subcontinent. This westerly bias is more pronounced in HiGEM1.2 and extends further into the north west Pacific. On the other hand HiGEM1.2 shows a reduced bias in the equatorial easterly Pacific trades, associated with the improvements in the east-west SST gradient. Over the southern oceans the notable feature is the reduction of the cyclonic anomaly to the west of South America in HiGEM1.2, which can be interpreted as a Rossby wave response to the improved heating pattern over the Indo-Pacific warm pool in the same manner that the NH wintertime circulation was improved.

Overall the impacts of higher resolution on the mean circulation in the atmosphere are felt mostly through the remote effects of the improved heating patterns over the Indo-Pacific warm pool. There are more subtle adjustments in the sub-tropical jets which can be linked to changes in storm track activity which will be described in more detail in Shaffrey *et al.* (2008).

### **3.4 Aerosols**

The interactive aerosol scheme in HiGEM1.2 is the same as for HadGEM1, described in Martin *et al.* (2006). No changes were made to the parametrisations in the aerosol schemes to allow for the increased horizontal resolution in HiGEM1.2, and differences in total global burdens were found to be small (<6%, see Table 2), indicating that the schemes are robust in this respect. However, there are some regional differences in the aerosol distributions in HiGEM1.2 and HadGEM1.2, as can be seen in Figure 11, which shows the annual mean column loadings of sulphate and biomass aerosols in HiGEM1.2 and differences from the HadGEM1.2 control. Some of the differences in aerosol

loadings are associated with changes in circulation between HiGEM1.2 and HadGEM1.2. In particular, the increases in sulphate aerosol over the North West Pacific may be related to increased advection from local sources over East and South Asia through intensification of the subtropical North Pacific jet (Figure 8) and stronger monsoon westerlies (Figure 10). Similarly, changes in biomass-burning aerosols over the North Tropical Atlantic appear to be related to a southward shift and intensification of the African Easterly Jet (Figure 10). However, the increase in sulphate aerosol around Antarctica in HiGEM1.2 is due to the reduction in sea ice relative to HadGEM1.2 (Figure 17), allowing more dimethyl sulphide to be emitted from the open sea surface.

Sulphate, black carbon, biomass-burning and sea-salt aerosols all feed back on the models via the direct radiative effect (scattering and/or absorption of radiation) and all but black carbon contribute to the first and second indirect effects (cloud albedo and precipitation efficiency, see IPCC 2007, Chapter 2). Figure 11 (bottom panel) shows the annual mean cloud droplet effective radius ( $r_e$ ) from HiGEM1.2 and differences from the HadGEM1.2 control. In both models,  $r_e$  is calculated as a function of the cloud liquid water content and the aerosol concentration (Jones *et al.* 2001). Martin *et al.* (2006, their Figure 18) show that the simulated distributions from HadGEM1 compare reasonably well with the satellite retrievals from Han *et al.* (1994). Differences between HiGEM1.2 and the new control HadGEM1.2 demonstrate a clear negative correlation between aerosol concentration and  $r_e$ , with more/less polluted air giving rise to smaller/greater values of  $r_e$ , e.g. across the Northern Pacific, off the East coast of Africa, and around Antarctica. In other regions, e.g. off the West coasts of Africa and South America, it is the improved representation of marine stratocumulus cloud in HiGEM1.2 (noted above) which affects values of  $r_e$ , as seen from the positive correlation with the reflected solar radiation (see Figure 2) in these areas.

An interactive dust scheme has not been included in this version of the model, but has been tested extensively in the atmosphere-only version, HiGAM1.2, where the increased atmospheric

resolution and improved surface topography have yielded very good results, especially for Saharan dust (see Woodage *et al.* 2008). Results suggest that including dust in the model might offset some of the cold land surface temperature errors over the Sahara shown in Figure 4.

### 3.5 Ocean

The increase in resolution for the ocean is more substantial than for the atmosphere, and a key question is whether the ability to permit the effects of eddies to be resolved more completely has a fundamental effect on the basic ocean circulation. Furthermore, the higher resolution allows a better representation of key aspects of the bathymetry, including channels and sills. The transports through important straits and passages around the worlds oceans are shown in Figure 12. There is a general improvement in the transports through the straits linking the Arctic to the south (Fram Strait, Denmark Strait, Iceland to Scotland Ridge System and Bering Strait). In particular the transport through the Fram Strait is much better represented in HiGEM1.2 than in the coarser resolution HadGEM1.2.

The modelled transports through the Florida Strait are lower than observed. This is primarily due to the poor representation of transports through the narrow passages which link the North Atlantic and the Caribbean Sea, and eventually feed into the Florida Current. In HiGEM1.2 and HadGEM1.2 the flow through the Windward Passage is northward out of the Caribbean Sea, whereas the observed flow is  $10.1 \pm 2.4 Sv$  southward into the Caribbean Sea (Johns *et al.* 2002). The strength and direction of the transport through the Windward Passage has been shown to be sensitive to the frictional effects associated with the narrow passages into the Caribbean Sea (Wajsowicz 2002), but even at  $1/10^\circ$  horizontal resolution, Maltrud and McClean (2005) found that the Florida Strait transport was weaker than observed, since most of the transport passed out of the Caribbean Sea via the Windward Passage. The Indonesian Through Flow provides a important

connection between the Pacific and Indian Oceans on both the local and large scale. Even at higher resolution it is still not possible to resolve the complex topography of this region, and the transports in both models exceed the observed values by 3-4  $Sv$ .

The strength of the Antarctic Circumpolar Current (ACC), as indicated by the transport through the Drake Passage, is 187Sv for HiGEM1.2 and 169Sv for HadGEM1.2. This is significantly higher than the  $138 \pm 13$  Sv found from observations (e.g. Naveira Garabato *et al.* 2003), but well within the range of values found within the CMIP3 coupled climate models (Russell *et al.* 2006). In both models the wind stresses over the Southern Ocean are too strong, which contributes to the excessive ACC transport. In addition, the ACC transport in HiGEM1.2 is somewhat stronger than that found in HadGEM1.2. The stronger transport in HiGEM1.2 is partly due to the *top to bottom* water mass transformations through deep convective events in the Ross and Weddell Seas associated with the formation of persistent polynyas during the first few decades of the HiGEM1.2 integration (see Section 3.6). The deep convective events act to increase the meridional density gradient and coincide with an upturn in the ACC transport in HiGEM1.2 (see Stevens *et al.* (2008) for more details).

Figure 13 shows the Atlantic overturning streamfunction for HiGEM1.2 and HadGEM1.2 overlaid with the zonal mean potential temperature differences from climatology (Conkright *et al.* 2002). Recent observational estimates from moored array instruments at  $26^\circ$  N, have been used to establish a relatively robust value for the Atlantic meridional overturning circulation of  $18.7 Sv \pm 5.6$  (Cunningham *et al.* 2007), which compares favourably with both the HadGEM1.2 ( $18.2 Sv \pm 3.0$ ) and HiGEM1.2 ( $19.5 Sv \pm 2.8$ ). The patterns of overturning streamfunction in both model are grossly similar, but there are a few minor differences. HiGEM1.2 has slightly weaker overturning than HadGEM1.2, and the overturning in HiGEM1.2 penetrates further into the Subpolar North Atlantic. The overturning in both models is relatively deep for a  $z$ -level model,

exceeding 3500 *m* in both models. Observational estimates at 26°N in the Atlantic suggest that below 3000m there is a 7.8Sv southwards flow (Cunningham 2007). This compares to the negligible southward flow below that depth seen in HadCM3 (Gordon et al 2000) and the approximately 4Sv southward flow in both HadGEM1.2 and HiGEM1.2. It is possible, however, there may be further changes in the deep Atlantic water-masses if the HiGEM1.2 and HadGEM1.2 integrations described here were extended.

The temperature differences from climatology are shown in Figure 13 (salinity errors are not shown but have a very similar spatial pattern). The high latitude dense overflows in HadGEM1.2 are too warm and salty, moreso than in the higher horizontal resolution HiGEM1.2 model. Z-level models have difficulty resolving the dense overflows in the northern North Atlantic (Beckmann and Doscher 1997) and coarser horizontal resolution will result in more spurious mixing in these sensitive regions. Figure 13 also shows the subsurface warming, mentioned previously in section 3.1, that develops in both HadGEM1.2 and HiGEM1.2 during the first few decades of the model integration.

Mesoscale eddy variability in the ocean is characterised by the sea surface height variability. To investigate how much variability is present in HiGEM1.2 and HadGEM1.2 the standard deviation in the model sea surface heights have been compared with satellite altimetry data (Figure 14). The satellite variability field is calculated from 3 years (1993-1995) of 10 day fields of sea surface height anomaly data from TOPEX/POSEIDON (AVISO, 1996, 1998; Le Traon *et al.* 1998), gridded at a resolution of  $\frac{1}{4}^{\circ}$  and therefore comparable to the resolution of HiGEM1.2. The model variability field is calculated as the standard deviation of 5 day mean sea surface height fields over years 21-70.

The observations (Figure 14a) show high levels of mesoscale eddy variability associated with the western boundary currents (e.g. the Gulf Stream, the Kuroshio and the Agulhas) and along the

Antarctic Circumpolar Current. Lower levels of variability are found in the eastern basins of the Pacific and Atlantic and in the Tropics. HadGEM1.2 with its low resolution does not explicitly permit eddies, except partially in the tropics where the resolution is increased in the meridional direction. The sea surface height variability (Figure 14b) is much lower everywhere than observations. This is to be expected as the baroclinic instability processes that form eddies are not represented.

Increasing the horizontal resolution to the eddy permitting  $1/3^\circ$  scale of HiGEM1.2 has enhanced the eddy activity in the ocean, and in places resolved larger scale eddy features (Figure 14c). The maximum values found along the western boundary currents and along the path of the Antarctic Circumpolar Current are comparable with observations. However, in common with other eddy permitting models (e.g. Maltrud and McClean, 2005; Hallberg and Gnanadesikan, 2006) there are a number of deficiencies. Regions of maximum variability tend to be spatially confined, since models of this resolution do not correctly propagate energy away from the high energy source regions. The Gulf Stream separates too far north with a persistent anticyclonic eddy. The eddies formed by the retroflexion of the Agulhas Current follow too similar paths into the South Atlantic, as indicated by the narrow path of high variability. These deficiencies are known to be improved with further increases in resolution (Maltrud and McClean, 2005, OCCAM  $1/12^\circ$ , <http://www.soc.soton.ac.uk/JRD/OCCAM/>). However, as will be shown later, the presence of these eddies in HiGEM1.2 and hence variations in SST on the same scale, leads to features in the atmosphere which have important implications for the fully coupled system.

The meridional heat transport by the oceans is a key factor in the accurate simulation of SSTs and indeed in the global energy cycle. The oceanic northward heat transports in HiGEM1.2 and HadGEM1.2 (Figure 15) are broadly comparable with the direct estimates of Ganachaud and Wunsch (2003) and the NCEP derived indirect estimates of Trenberth and Caron (2001). Note however,

that there is considerable uncertainty in the observational estimates. The global peak poleward heat transports produced by both models are weaker than the observations though within the range of uncertainty. The peak northward heat transport is 1.13 PW for HiGEM1.2 and 1.26 PW for HadGEM1.2 compared with estimates of 1.18 PW by Trenberth and Caron (2001) and 1.27 PW by Ganachaud and Wunsch (2003). The lower value for HiGEM1.2 is consistent with its slightly weaker meridional overturning circulation (Figure 13) and weaker overturning component of the heat transport. North of 40°N the northward heat transport is too large in both models for both the Atlantic and the global ocean. This is largely due to overly vigorous subpolar gyres, as evidenced by the large gyre component of the heat transport that dominates the northern North Atlantic (Figure 15a). A partial explanation for the strong subpolar gyre transports may be the excessively strong westerly winds over the North Atlantic Ocean seen in both HadGEM1.2 and HiGEM1.2 (e.g. Figure 7).

Both HadGEM1.2 and HiGEM1.2 exhibit a convergence of heat on to the equator due to eddy heat transport (actually all transient motions  $\overline{v'T'}$ ) (Figure 15(b)). This convergence is somewhat larger at higher resolution since tropical instability waves, which flux heat towards the equator, are better resolved by HiGEM1.2 (see Section 4.1). The larger convergence of heat is partially responsible for the improved simulation of equatorial SSTs seen at higher resolution, alleviating the cold SST errors in the equatorial Pacific (Roberts *et al.* 2008a), and which are common in climate models without flux correction (Guilyardi 2006).

The other region where the eddies play an important role in transporting heat is the Southern Ocean. Here the eddy component is negligible in HadGEM1.2, whereas it fluxes up to 0.5 PW poleward in HiGEM1.2. As can be seen in Figure 14, eddy variability is negligible in the Southern Ocean for HadGEM1.2. The diffusive component in HadGEM1.2, however, includes the eddy parametrisation of Gent and McWilliams (1990) which appears to provide a reasonable

representation of the heat transport from the partially resolved eddies of HiGEM1.2.

Overall, the impact of increased resolution in the ocean component of HiGEM1.2 has been relatively small in terms of the overall global heat transport and mean overturning circulation. However, it is clear that the capability to represent ocean eddies and strong SST gradients in key regions, such as the eastern equatorial Pacific and the Gulf Stream, has a significant impact on the heat budget of the Tropical Pacific (Roberts *et al.* 2008a) and the North Atlantic. In turn this leads to important improvements in the mean climate of these regions, which has both global implications and substantial impacts on the regional weather and climate variability.

### **3.6 Sea ice**

As noted in Section 2.4, the sea ice component in HadGEM1 is based around the CICE elasto-viscous-plastic model (Hunke and Lipscomb 2004), and a more detailed description of the sea ice model and comprehensive evaluation against observations is given in McClaren et al (2006). The seasonal evolution and distribution of sea ice area and fraction in HiGEM1.2 and HadGEM1.2 is compared with those derived from satellite passive microwave observations using the bootstrap algorithm (Comiso 1999) for the Northern and Southern Hemispheres. Figures 16 and 17 show the distributions of sea ice fraction in the Northern and Southern Hemispheres for the months of March and September (i.e the months of maximum/minimum extent) for HiGEM1.2, HadGEM1.2 and observations. Overall there is greater sea ice area in HadGEM1.2 than in HiGEM1.2 in both hemispheres, which is consistent with the global mean surface temperatures being colder in HadGEM1.2.

The amplitude of the seasonal cycle of NH sea ice area (not shown) is larger than observations in both models. The net result is that the magnitude of the sea ice area is well modelled in HiGEM1.2 in wintertime but underestimated in summertime. On the other hand, consistent

with the results of HadGEM1 (McClaren 2006), the wintertime sea ice area is overestimated in HadGEM1.2 while the summertime modelled sea ice area is close to that observed. For all months in the Southern Hemisphere, the sea ice area is severely underestimated in HiGEM1.2, but overestimated in HadGEM1.2.

In terms of the spatial distribution of sea ice fraction, the Northern Hemisphere fraction looks realistic in HiGEM1.2, but the sea ice melts back too far in September, particularly along the Russian coastline in the Arctic Sea. In HadGEM1.2 there is too much sea ice in March, particularly in the Labrador Sea, around the Bering Straits and in the Sea of Okhotsk. Even though the total September sea ice area in HadGEM1.2 is comparable with observations, Figure 16 shows that there is too much sea ice in the Labrador Sea and not enough in the central Arctic.

For the Southern Hemisphere, although the total sea ice area in September in HadGEM1.2 is overestimated, the actual values of sea ice fraction are lower than the observed values over most of the Antarctic. In HiGEM1.2 the underestimation of Antarctic sea ice can be clearly seen by comparing the observed and modelled distributions of sea ice fraction (Figure 17). The most striking feature of the September distribution of sea ice in HiGEM1.2 is the lack of ice in the Ross and Eastern Weddell Seas, which, in individual years, appears as persistent open-ocean polynyas. These polynyas start to appear in year 8 of the run and, by year 14, much of the winter ice cover has disappeared from the Ross and Weddell Seas. The sea ice cover in the Weddell Sea starts to recover and, by year 21, a more realistic winter ice cover is reestablished. In the Ross Seas, however, sea ice fractions remain low although they partially recover in the last few decades of the run (Figure 1f).

Once the polynyas have appeared in the Weddell and Ross Seas, strong local feedbacks discourage the sea ice from reforming. In particular, an increased surface heat flux over the polynya region leads to increased ocean convection and entrainment of relatively warm and salty deep water

into the upper ocean. The homogenisation of the water column, and warming of the upper ocean by convection discourages sea ice formation, and the weak ocean stratification implies that an extensive heat loss from the polynya region is required before sea ice can reform. It is also possible that other local feedbacks such as sea ice import/export into the polynyas or the coupled ocean-atmosphere feedback described by Timmerman *et al.* (1999) might play a role in maintaining the open-ocean polynya in HiGEM1.2. Although open-ocean polynyas with multi-annual persistence have been observed in the Weddell Sea (Gordon and Comiso 1988), it is unclear why they form so readily in HiGEM1.2. This issue will be dealt with in greater depth in a later paper.

The lack of Antarctic sea ice in HiGEM1.2 has a large impact both globally and locally on the model. The reduction in sea ice results in a reduction in surface albedo and an increase in net surface solar radiation and so a warming of the upper ocean of the Southern Hemisphere, particularly in Austral summertime. This can be seen, for example, in the difference in the SSTs between HiGEM1.2 and observations (Figure 3). It is also worth pointing out that the underestimation of sea ice in HiGEM1.2 has a global impact on the model. As noted in section 3.1 the differences in Antarctic sea ice, along with the differences in total cloud amount, result in a reduction in the global albedo of HiGEM1.2 and contribute to the slight positive bias in the net TOA radiation (Table 1). The gradual reformation of sea ice around Antarctica during the run also leads to slow reduction in net surface solar and net TOA in the later part of the HiGEM1.2 integration.

Sea ice has proved to be the most challenging part of the development of HiGEM1.2, and although some aspects of the results show improvements in the simulation, the possibility for new feedbacks involving the formation of polynyas has raised a number of new and interesting research questions about the coupled behaviour of the ocean-sea ice-atmosphere system and the potential for the coupled system to rapidly lose ice as a result of non-linear feedbacks, which merit further investigation.

## 4. Atmosphere-ocean coupling

In the previous section the time-mean state of the individual components of HiGEM1.2 were evaluated against HadGEM1.2 and observations. One interesting aspect of HiGEM1.2 is whether the local interactions that occur on smaller scales between components have a significant impact upon the model. In particular, one important question that is raised is whether the smaller scale features that can be resolved by the eddy-permitting ocean in HiGEM1.2 have an impact on the high resolution atmosphere. This section describes a number of examples of where such small-scale ocean atmosphere interactions are important.

### 4.1 Tropical Instability Waves

Since HiGEM1.2 has a high resolution atmosphere coupled to a high resolution ocean, it can simulate local, coupled air-sea interactions on relatively fine scales. One of the scales that is resolved by HiGEM1.2 is the interaction of Tropical Instability Waves (TIWs) with the tropical atmosphere, an interaction that has been inferred from satellite observations of surface wind stresses for some time (Hashizume *et al.* 2001, Chelton *et al.* 2001). TIWs are mixed barotropic-baroclinic instabilities that form in the tropical counter-current system. In the tropical East Pacific Ocean, TIWs can be seen forming along SST gradients and strong shears flanking the cold tongue, and then travelling westwards along the SST gradient.

TIWs are associated with substantial SST anomalies that can then have an impact on fluxes of moisture and heat into the atmosphere. The warming of the boundary layer, and subsequent decrease in static stability associated with a warm SST anomaly will act to increase the vertical mixing of momentum, so that warm SST anomalies will be associated with an increase in surface winds (Wallace *et al.* 1989). However, observations (Cronin 2003) have also suggested that TIWs

are associated with surface pressure anomalies, thus a component of the surface wind response will be forced by pressure gradients (Linzden and Nigam 1987).

Oceanic TIWs have previously been resolved by ocean-only models and high resolution ocean (but standard atmosphere resolution) coupled models (Roberts *et al.* 2004), and the impact of TIWs on the atmosphere has only been studied in high resolution atmosphere-only integrations (Small *et al.* 2003). Coupled ocean-atmosphere models have not had sufficient resolution to resolve the small-scale coupled interaction between TIWs and the tropical atmosphere. Figure 18b shows instantaneous Equatorial Pacific SSTs and windstress divergence from HadGEM1.2. Some TIW activity is resolved along the Tropical Pacific cold tongue in HadGEM1.2 where the meridional ocean resolution is enhanced, and where there are strong SST fronts, there is some indication of an atmospheric response. However, the low level of TIW activity in HadGEM1.2 contrasts with that found in HiGEM1.2 (Figure 18a), which shows a series of TIWs along the northern, and to a lesser extent the southern flanks of the cold tongue. The structure of the TIWs in HiGEM1.2 compares favourably with that seen from TMI SST satellite imagery (Chelton *et al.* 2001). The structure of the atmospheric response to the TIWs is also very similar to that seen in QuikSCAT imagery with regions of windstress divergence seen along the cross-wind SST fronts, suggesting that HiGEM1.2 is capable of simulating the coupled small-scale interactions between oceanic TIWs and the tropical atmosphere.

There is good evidence to believe that the faithful representation of the TIWs and the associated atmospheric response in HiGEM1.2 are essential components of the marked improvement in the SSTs in the central and east equatorial Pacific and hence in the east-west temperature gradient. As discussed in Roberts *et al.* (2008a) and Harle *et al.* (2008), the TIWs act to mix heat both zonally and meridionally in to the cold tongue region thereby improving the local heat budget and the structure of the thermocline. Furthermore, the atmospheric response to the TIWs acts to break

up the strong easterly trades in the model and potentially reduce the positive feedback between easterly windstress, ocean upwelling and cold SSTs.

One question raised by these results is how the interaction between TIWs and the atmosphere in HiGEM1.2 might be parametrised in a lower resolution model such as HadGEM1.2. Developing such a parametrisation would be difficult since it would need to be sufficiently complex to capture the nature of this coupled interaction, which emerges from being able to resolve motions in both ocean and atmosphere at the appropriate scale, and also realistically representing the small scale non-linear fluxes of heat, moisture and momentum between components.

## **4.2 ENSO Variability**

One of the most important results of this study is the marked improvement in the simulation of El Nino and its global influence in HiGEM1.2. Figure 19 shows the monthly Nino3.4 SST timeseries from the 70 year integrations of HiGEM1.2 and HadGEM1.2, as well as the power spectra for Nino3 from the extended integrations of HiGEM1.1/HadGEM1.1 on the Earth Simulator. The spectra also include two estimates from observations including one for the latter half of the 20th century which would be more commensurate with the current GHG forcing used in the simulations. The spectra have been normalised in terms of the peak power and the figure also includes the standard deviation of the Nino3 SSTs.

As described by Johns *et al.* (2006) and evident in Figure 20, El Nino events in HadGEM1.2 are smaller in magnitude and less coherent in structure than in the observations. This can be attributed to the excessively strong easterly windstresses in the model that induce too much upwelling of cold water along the Equatorial Pacific and confine the convective activity to the Maritime Continent. This means that the air-sea interaction and relaxation of the trades which lie at the heart of El Nino is inhibited in HadGEM1.2.

The corresponding 70 year Nino 3.4 SST timeseries from HiGEM1.2 is shown in Figure 19b. At the beginning of the integration there is a series of strong anomalies that indicate the model adjustment in the Tropical Pacific. Thereafter, there is much more interannual variability in HiGEM1.2 than in HadGEM1.2, as is evident also in the higher standard deviation for Nino3. Figure 19 also shows that large positive SST anomalies in the Tropical Pacific are greater than the large negative anomalies, a characteristic seen in the observations, although the HiGEM1.2 timeseries is not as skewed as observed.

The power spectra from the extended integrations confirm the substantial improvement in El Nino implied by the timeseries. In HadGEM1.1 there is very little power at the frequencies generally associated with El Nino whereas in HiGEM1.1 there is a strong spectral peak between 3 and 5 years. The reasons for the dramatic shift in El Nino timescales between HadGEM1.1 and HiGEM1.1 is discussed in detail in Roberts *et al.* (2008b).

The difference in El Nino between HadGEM1.2 and HiGEM1.2 is further highlighted by composites of DJF SST and precipitation (Figure 20) based on the 8 largest El Nino events (after year 20), as measured by the DJF Nino3.4 SST anomalies. Relative to HadGEM1.2, the representation of El Nino is substantially improved in HiGEM1.2. In comparison to observations the DJF El Nino SST composite anomalies in HadGEM1.2 is weaker than observed, particularly in the East tropical Pacific, whereas the El Nino SSTs in HiGEM1.2 have a spatial pattern and amplitude much closer to that observed. However, the El Nino SSTs still extend too far into the West Tropical Pacific, which is a common failing of most climate models (Guilyardi *et al.* 2004).

The DJF precipitation composite anomalies for the models and observations (Figures 20b, d and e) also indicate that the distribution of precipitation during an El Nino event in HiGEM1.2 is closer to observations than in HadGEM1.2. In HadGEM1.2 the precipitation over West Pacific does not move as far eastwards into the central Pacific as it does in HiGEM1.2 and the observations,

due to the strong negative SST biases in that region. However, there are still significant differences between observations and HiGEM1.2, particularly over the West Pacific where the absolute SSTs are erroneously warm and are able to continue to support strong convection even during an El Nino event. In terms of tropics-wide teleconnections, it is notable that HiGEM1.2 is able to capture some aspects of the observed remote response of precipitation during an El Nino event, suggesting the model has some skill in replicating the observed transitions of the Walker Circulation. For example, the excessive response over the Indian Ocean in HadGEM1.2 is much improved in HiGEM1.2.

The improvements in the precipitation response to El Nino in HiGEM1.2 translate into a significantly better simulation of the global ENSO teleconnections. Figure 21 shows the DJF composite mean sea level pressure anomalies from ERA-40 and both simulations. HiGEM1.2 has successfully captured the deepening of the Aleutian Low and the response over the Eurasian sector during El Nino events. However, the deepening of the Aleutian Low in HiGEM1.2 occurs to the west of the observations, which may be related to the rainfall not moving as far eastwards into the central Tropical Pacific (Spencer and Slingo 2002). The response in the Northern Hemisphere in HiGEM1.2 is in stark contrast to that seen in HadGEM1.2, which fails to capture the observed extratropical teleconnections during an El Nino.

## **5. Concluding Discussion**

This paper describes the development and basic performance in a multi-decadal simulation of the UK's new high resolution global coupled model, HiGEM. More detailed analyses of specific aspects of the simulations will be presented in subsequent papers. Nevertheless there are some important conclusions that can be drawn from this study.

Unlike most resolution studies, which have been largely based on atmosphere-only or ocean-

only models, or on increased resolution in one component only, this is one of the first times that the resolution of both components has been increased simultaneously. This is an important point because a previous study by Roberts *et al.* (2004), in which only the ocean component was taken to higher resolution ( $1/3^\circ$  as here), showed very little impact on the mean climate of the coupled model. One of the most striking results of this study is that when the atmosphere resolution is also increased, then the atmosphere is able to respond to the fine-scale detail in the SST field in a coherent way, with important implications for the mean climate and its variability. For example, it has been shown that tropical instability waves and the response to them of the near surface winds, both now well resolved in HiGEM, have a significant effect on the mean state of the equatorial Pacific Ocean and hence on the global mean climate and ENSO (Roberts *et al.* 2008a,b).

The existence of coherent coupling between the ocean and atmosphere on fine spatial scales and on relatively short timescales challenges the conventional approach to climate modelling which assumes that sub-gridscale processes can be parametrised within a single component of the system. The results from HiGEM suggest that there may be important scales of *coupled* behaviour that cannot be parametrised and that will therefore need to be resolved adequately. The implication of this is that there may be a minimum resolution for modelling the *coupled* system that may be higher than, or at least different from that for the individual components. This also means it may be important for the atmosphere and ocean components of coupled models to have resolutions that are roughly equivalent, so that the atmosphere can respond to, and in turn force the ocean on commensurate time and space scales.

The multi-scale nature of the coupled processes demonstrated by HiGEM also has wider implications for the extension of physical climate models to full earth system models. As a demonstration of this point, Figure 22 compares the annual mean surface windstress curl and SSTs observed by QuikSCAT (Risien and Chelton, 2008) and simulated by HiGEM1.2 and HadGEM1.2. The

windstress curl is important for forcing upwelling in the ocean which is critical for biological production. In the QuikSCAT observations there is considerable structure in the windstress curl along coasts, around islands and in association with strong SST gradients (e.g. Gulf Stream) and large ocean eddy activity (e.g. Southern Oceans). Many of these features are captured well by HiGEM1.2, but to a much lesser extent by HadGEM1.2, particularly those associated with islands and persistent small-scale SST structures (e.g. oceanic fronts). These deficiencies could be important when the model is coupled to ocean biology where the strength of upwelling regions are crucial for providing nutrients.

Figure 22 demonstrates again that the atmosphere in HiGEM1.2 is capable of responding to small scale structures in the SST in a more realistic way, as has already been shown for tropical instability waves. Important features such as the Gulf Stream and the windstress curl associated with it are better represented in HiGEM, with tighter SST gradients and a more realistic orientation; in HadGEM1.2 the Gulf Stream is too zonal and the region of high SST gradients extends too far into the Atlantic Ocean.

Although HiGEM has demonstrated substantial benefits for some aspects of the climate system and its variability, some significant model problems remain, and some new ones have emerged. Errors in tropical rainfall patterns are particularly stubborn and are largely unaffected by increased resolution, apart from some improvements over the Warm Pool associated with a better simulation of the equatorial Pacific SSTs. It is becoming clear that current approaches to parametrising tropical convection may be inadequate for representing the strong physical-dynamical coupling involved in the organised convection that forms the basis of tropical weather systems (e.g. Slingo *et al.* 2003). This organisation occurs on scales much smaller than most global models can hope to represent at the current time. So increasing resolution is not a panacea for all climate model errors, and much fundamental research on physical parametrisations, especially convection, remains to be

done.

One of the most challenging aspects of developing HiGEM was the complexity of representing sea ice in a high resolution coupled system. Considerable work was needed to reach a stable solution and even then the model has produced unexpected non-linear feedbacks that have resulted in a substantial loss of Antarctic sea ice, particularly in the Ross Sea. The formation of large and persistent polynyas in HiGEM led to a chain of responses which affected the Antarctic Ocean circulation and the subsequent ability of the system to form seasonal sea ice. In the last decade or so of the simulation the sea ice is recovering, which provides an opportunity to analyse these feedbacks in more detail. It is interesting to note that the development of large multi-year polynyas is observed in the real system, for example in the Weddell Sea during the 1970s, and it is possible that instabilities, such as those demonstrated by HiGEM, may be one way in which Antarctic sea ice may evolve in the future. This demonstrates again the importance of exploring high resolution coupled processes to find out whether there are non-linear feedbacks in the climate system that have hitherto been undetected in low resolution models.

The development of HiGEM to produce a coupled model capable of stable multi-decadal simulations presented a much bigger challenge than originally anticipated because of issues of numerical stability and computational performance. The computational resource required for such models is still at the limit of what is feasible for the long production runs required for climate change projections. However, there is sufficient computer power now for a systematic exploration of the importance of model resolution in the atmosphere and ocean, together, for simulating the coupled climate system. In the next phase of HiGEM the intention is to further increase the atmospheric resolution to bring it even closer to that of the ocean. It is only by undertaking these kinds of studies that the validity of lower resolution climate models can be tested. At the same time, taking models to higher resolution enables a much more meaningful comparison with the wealth

of satellite data that exists on scales much finer than those currently used in models.

## **Acknowledgements**

The support of NERC through the UK-HiGEM project and the UK-Japan Climate Collaboration is acknowledged. The Met Office Hadley Centre also acknowledges the support of the UK-Japan Climate Collaboration through the Joint DEFRA and MoD Integrated Climate Programme - GA01101, CBC/2B/0417- Annex C5.

This work made use of the facilities of HPCx, the UK Research Councils' national high performance computing service, which is provided by EPCC at the University of Edinburgh and by CCLRC Daresbury Laboratory, and funded by the Office of Science and Technology through EPSRC's High End Computing Programme. Computing time at the Earth Simulator was kindly provided by JAMSTEC through the UK-Japan Climate Collaboration. Data archiving and distribution was provided by the British Atmospheric Data Centre.

The authors would also like to Alison McLaren, Ann Keen, and Manoj Joshi for their useful comments and support during the development of UK-HiGEM.

## References

- Andres, R. J., and A. D. Kasgnoc, 1998: A time-averaged inventory of subaerial volcanic sulphur emissions. *J. Geophys. Res.*, **103**, 25251-25261.
- AVISO, 1996: AVISO User Handbook: Merged TOPEX/POSEIDON Products. AVI-NT-02-101-CN, Edition 3.0, CNES, Toulouse.
- AVISO, 1998: AVISO User Handbook: Sea Level Anomalies (SLAs). AVI-NT-011-312-CN, Edition 3.1, CNES, Toulouse.
- Baringer, M. O. and Larsen, J. C., 2001: Sixteen years of Florida Current transport at 27°N, *Geophysical Research Letters*, **28**, 3179-3182.
- Beckmann, A. and Doscher, R., 1997: A method for improved representation of dense water spreading over topography in geopotential-coordinate models, *Journal of Physical Oceanography*, **27**, 581-591.
- Bryan, F.O. and W. R. Holland, 1989: A high-resolution simulation of the wind- and thermohaline-driven circulation of the North Atlantic Ocean. Parameterisation of Small-Scale Processes. Proceedings 'Aha Huliko'a, Hawaiian Winter Workshop, P. Muller and D. Henderson, Editors, Hawaii Inst. Geophys. Spec. Publ., 99-115.
- Chelton, D. B., S. K. Esbensen, M. G. Schlax, N. Thum, M. H. Freilich, F. J. Wentz, C. L. Gentemann, M. J. McPhaden and P. S. Schopf, 2001: Observations of coupling between surface wind stress and sea surface temperature in the eastern Tropical Pacific. *J. Climate*, **14**, 1479-1498.
- Chelton, D. B., M. G. Schlax, M. H. Freilich and R. F. Milliff, 2004: Satellite measurements reveal persistent small-scale features in ocean winds. *Science*, **303**, 978-983.
- Clark et al, 2008: UK-HiGEM: The New UK High Resolution Global Environment Model. Land surface modelling. *To be submitted to J. Geophys. Res.*

- Collins, W. J., D. S. Stevenson, C. E. Johnson, and R. G. Derwent, 1997: Tropospheric ozone in a global-scale three-dimensional Lagrangian model and its response to NO<sub>x</sub> emission controls. *J. Atmos. Chem.*, **26**, 223-274.
- Comiso, J.C., 1999 (updated 2005): Bootstrap sea ice concentrations for NIMBUS-7 SMMR and DMSP SSM/I. Boulder, CO, USA: National Snow and Ice Data Center. Digital media.
- Conkright, M. E. and Locarnini, R. A. and Garcia, H. E. and O'Brien, T. D. and Boyer, T. P. and Stephen, C. and Antonov, J. I., 2002: World Ocean Atlas 2001: Objective Analyses, Data Statistics, and Figures, CD-ROM Documentation, National Oceanographic Data Center, Silver Spring, MD, 17pp.
- Cronin, M. F., S.-P. Xie and H. Hashizume, 2003: Barometric pressure variations associated with eastern Pacific tropical instability waves. *J. Climate*, **16**, 3050-3057.
- Cunningham, S. A. and Alderson, S. G. and King, B. A. and Brandon, M. A., 2003: Transport and variability of the Antarctic Circumpolar Current in the Drake Passage, *Journal of Geophysical Research*, **108**, doi:10.1029/2001JC001147.
- Cunningham S.A., Kanzow T., Rayner D., Baringer M.O., Johns W.E., Marotzke J., Longworth H.R. Grant E.M., Hirschi J.J.-M., Beal L.M., Meinen C.S., and Bryden H.L., 2007: Temporal variability of the Atlantic Meridional Overturning Circulation at 26°N. *Science*, **317**, 935-938.
- Davies, T., M. J. P. Cullen, A. J. Malcolm, M. H. Mawson, A. Staniforth, A. A. White, and N. Wood 2005: A new dynamical core for the Met Office's global and regional modelling of the atmosphere. *Quart. J. Roy. Meteor. Soc.*, **131**, 1759-1782.
- Dukowicz, J. K. and R. D. Smith, 1994: Implicit free surface method for the Bryan-Cox-Semtner ocean model. *J. Geophys. Res.*, **99**, 7991-8014.
- Fahrbach, E. and Meincke, J. and Österhus, S. and Rohardt, G. and Schauer, U. and Tverberg, V. and Verduin, J. and Woodgate, R.A., 2001: Direct measurements of heat and mass transports

- through the Fram Strait, *Polar Research*, **20**, 217-224.
- Feistel, R. and E. Hagen, 1995: On the Gibbs thermodynamic potential of seawater. *Prog. Oceanog.*, **36**, 249-327.
- FRAM Group, 1991: An Eddy-Resolving Model of the Southern Ocean. *EOS Transactions , American Geophysical Union*, **72**, 169, 174-175.
- Ganachaud, A. and C. Wunsch, 2003: Large-Scale Ocean Heat and Freshwater Transports during the World Ocean Circulation Experiment, *J. Climate*, **16**, 696-705.
- Gent, P. R. and J. C. McWilliams, 1990: Isopycnal mixing in ocean circulation models. *J. Phys. Oceanog.*, **20**, 150-155.
- Gordon, A. L., and J. C. Comiso, Polynyas in the Southern Ocean, 1998: *Scientific American*, **256**, 90-97.
- Gordon, A.L.: 2001, Ocean Circulation and Climate, G. Siedler, J. Church, and J. Gould (Eds.), 303-314.
- Gordon, C., Cooper, C., Senior, C.A., Banks, H., Gregory, J.M., Johns, T.C., Mitchell, J.F.B., and Wood, R.A, 2000: The simulation of SST, sea ice extents and ocean heat transports in a version of the Hadley Centre coupled model without flux adjustments. *Climate Dynamics*, **16**, 147-168.
- Gill, A., 1982: Atmosphere-Ocean Dynamics, International Geophysics Series, Vol 30, Academic Press, London, 662 pp.
- Griffies, S. M., A. Gnanadesikan, R. C. Pacanowski, V. D. Larichev, J. K. Dukowicz and R. D. Smith, 1998: Isonutral diffusion in a z-coordinate ocean model. *J. Phys. Oceanog.*, **28**, 805-830.
- Guilyardi E., S. Gualdi, J. M. Slingo, A. Navarra, P. Delecluse, J. Cole, G. Madec, M. Roberts, M. Latif, and L. Terray, 2004: Representing El Nino in coupled ocean-atmosphere GCMs: The dominant role of the atmosphere. *J. Climate*, **17**, 4623-4629.

- Guilyardi E., 2006: El Nino-mean state-seasonal cycle interactions in a multi-model ensemble. *Clim. Dyn.*, **26**, 329-348.
- Guo, Z.C. and P.A. Dirmeyer, 1996: Evaluation of the Second Global Soil Wetness Project soil moisture simulations: 1. Intermodel comparison. *Journal of Geophysical Research* , **111**, doi:10.1029/2006JD007233.
- Hallberg, R., and A. Gnanadesikan, 2006: The role of eddies in determining the structure and response of the wind-driven Southern Hemisphere overturning: Results from the Modeling Eddies in the Southern Ocean (MESO) project. *J. Phys. Oceanogr.*, **36**, 2232-2252.
- Han, Q., W. B. Rossow and A. A. Lacis, 1994: Near-global survey of effective droplet radii in liquid water clouds using ISCCP data. *J. Climate*, **7**, 475-497.
- Hansen, B. and Österhus, S., 2000: North Atlantic-Nordic Seas exchanges, *Progress in Oceanography*, **45**, 109-208.
- Harle, J., A.L. New, L.C. Shaffrey, D.P. Stevens and I. Stevens, 2008: UK-HiGEM: Tropical Instability Wave air-sea coupling in the eastern equatorial Pacific. *To be submitted to J. Climate*.
- Hashizume, H., S.-P. Xie, W. T. Liu, and K. Takeuchi, 2001: Local and remote atmospheric response to tropical instability waves: A global view from space, *J. Geophys. Res.*, **106**, 10173-10185.
- Holdcroft, C., W.M.F. Grey, M. Barnsley, C.M. Taylor, S.O. Los, P.R.J. North, 2008: New vegetation albedo parameters and global fields of background albedo derived from MODIS for use in a climate model. *Submitted to J. Hydrometeorol*.
- Holland, D. M., 2001: An impact of subgrid-scale ice-ocean dynamics on sea ice cover. *J. Climate*, **14**, 1585-1601.
- Hoskins, B. J. and Karoly, D. J., 1981: The Steady Linear Response of a Spherical Atmosphere to Thermal and Orographic Forcing. *J. Atmos. Sci.*, **38**, 1179-1196.

- Huffman, G.J., R.F. Adler, D.T. Bolvin, G. Gu, E.J. Nelkin, K.P. Bowman, Y. Hong, E.F. Stocker, D.B. Wolff, 2007: The TRMM Multi-satellite Precipitation Analysis: Quasi-Global, Multi-Year, Combined-Sensor Precipitation Estimates at Fine Scale. *J. Hydrometeor.*, **8**, 38-55
- Hunke, E. C. and J. K. Dukowicz, 1997: An elastic-viscous-plastic model for sea ice dynamics. *J. Phys. Oceanog.*, **27**, 1849-1867.
- Hunke, E. C. and W. H. Lipscomb, 2004: CICE: The Los Alamos Sea Ice Model, documentation and software, Version 3.1, LA-CC-98-16. Los Alamos National Laboratory, Los Alamos, NM, 56pp.
- IOC, IHO and BODC, 2003: Centenary Edition of the GEBCO Digital Atlas, published on CD-ROM on behalf of the Intergovernmental Oceanographic Commission and the International Hydrographic Organization as part of the General Bathymetric Chart of the Oceans, British Oceanographic Data Centre, Liverpool, U.K.
- IPCC, 2007: Climate Change 2007: The Physical Science Basis. Contribution of Working Group I to the Fourth Assessment Report of the Intergovernmental Panel on Climate Change, Solomon, S., D. Qin, M. Manning, Z. Chen, M. Marquis, K.B. Averyt, M. Tignor and H.L. Miller (eds.), Cambridge University Press, Cambridge, United Kingdom and New York, NY, USA, 996 pp.
- Johns, T. C. and Coauthors, 2006: The New Hadley Centre Climate Model (HadGEM1): Evaluation of Coupled Simulations. *J. Climate*, **19**, 1327-1353.
- Johns, W. E. and Townsend, T. L. and Fratantoni, D. M. and Wilson, W. B., 2002: On the Atlantic inflow to the Caribbean Sea, *Deep Sea Research*, **49**, 211-243.
- Jones, A., D. L. Roberts, M. J. Woodage and C. E. Johnson, 2001: Indirect sulphate aerosol forcing in a climate model with an interactive sulphur cycle. *J. Geophys. Res.*, **106**, 20293-20310.
- Jónsson, S. and Briem, J., 2003: Flow of Atlantic Water west of Iceland and onto the north Icelandic Shelf, *ICES Marine Science Symposia*, **219**, 326-328.

- Jung T., Gulev S.K., Rudeva I., Soloviov V., 2006: Sensitivity of extratropical cyclone characteristics to horizontal resolution in the ECMWF model. *Quarterly Journal of the Royal Meteorological Society*, **132** 1839-1857.
- K-1 Model Developers, 2004: K-1 coupled model (MIROC) description, K-1 Tech. Rep. 1, edited by H. Hasumi and S. Emori, 34 pp., Cent. for Clim. Syst. Res., Univ. of Tokyo, Tokyo.
- Kiehl, J. T. and K. E. Trenberth, 1997: Earth's annual global mean energy budget. *Bull. Amer. Meteorol. Soc.*, **78**, 197-208.
- Kettle, A. J., and Coauthors, 1999: A global database of sea-surface dimethylsulfide (DMS) measurements and a procedure to predict sea surface DMS as a function of latitude, longitude and month. *Global Biogeochem. Cycles*, **13**, 399-444.
- Kushnir, Y., W.A. Robinson, I. Blade, N.M. Hall, S. Peng and R. T. Sutton, 2002: Atmospheric response to extratropical SST anomalies: A synthesis and evaluation of recent results. *Journal of Climate*, **15**, 2233-2256.
- Le Traon, P.Y., Nadal, F., Ducet, N., 1998. An improved mapping method of multi-satellite altimeter data. *J. Atmos. Oceanic Tech.*, **16**, 522-534.
- Linzden, R. S. and S. Nigam, 1987: On the role of sea surface temperature gradients in forcing low-level winds and convergence in the tropics, *J. Atmos. Sci.*, **44**, 2418-2436.
- Lipscomb, W. H., 2001: Remapping the ice thickness distribution in sea ice models. *J. Geophys. Res.*, **106**, 13989-14000.
- Loveland, T.R. , B. C. Reed, J. F. Brown, D. O. Ohlen, Z. Zhu, L. Yang, and J. W. Merchant, 2000: Development of a global land cover characteristics database and IGBP DISCover from 1 km AVHRR data. *Int. J. Remote Sens.*, **21**, 1303-1330.
- Ma, C.-C., C. R. Mechoso, A. W. Robertson and A. Arakawa, 1996: Peruvian stratus clouds and the tropical Pacific circulation - a coupled ocean-atmosphere GCM study. *J. Climate*, **9**, 1635-

1645.

- Macrander, A. and Send, U. and Valdimarsson, H. and Jónsson, S. and Käse, R. H., 2005: Interannual changes in the overflow from the Nordic Seas into the Atlantic Ocean through Denmark Strait, *Geophysical Research Letters*, **32**, doi:10.1029/2004GL021463.
- Marti, O., G. Madec and P. Delecluse, 1992: Comment on "Net diffusivity in Ocean General Circulation Models with Nonuniform grids" by F. L. Lin and I. Y. Fung. *J. Geophys. Res.*, **97**, 12763-12766.
- Maltrud, M. E. and McClean, J.L., 2005: An eddy resolving global 1/10° ocean simulation. *Ocean Modelling*, **8**, 31-54.
- Martin, G. M., M. A. Ringer, V. D. Pope, A. Jones, C. Dearden, and T. J. Hinton, 2006: The Physical Properties of the Atmosphere in the New Hadley Centre Global Environmental Model (HadGEM1). Part I: Model Description and Global Climatology. *J. Climate*, **19**, 1274-1301.
- McDougall, T. J., D. R. Jackett, D. G. Wright and R. Feistel, 2003: Accurate and computationally efficient algorithms for potential temperature and density of seawater. *J. Atmos. Oceanog. Tech.*, **20**, 730-741.
- McLaren, A. J., H. T. Banks, C. F. Durman, J. M. Gregory, T. C. Johns, A. B. Keen, J. K. Ridley and M. J. Roberts, 2006: Evaluation of the sea ice simulation in a new coupled atmosphere-ocean climate model (HadGEM1). *J. Geophys. Res.*, **111**, 12014-12031.
- Naveira Garabato, A.C., D.P. Stevens and K.J. Heywood, 2003: Water Mass Conversion, Fluxes, and Mixing in the Scotia Sea Diagnosed by an Inverse Model. *J. Phys. Oceanogr.*, **33**, 2565-2587.
- New, M., Lister, D., Hulme, M. and Makin, I., 2002: A high-resolution data set of surface climate over global land areas. *Climate Research*, **21**, 1-25
- Pacanowski, R.C. and S.M. Griffies, 1998: MOM3.0 manual. NOAA/GFDL, Princeton, NJ,

692pp.

- Pope, V. D., and R. A. Stratton, 2002: The processes governing horizontal resolution sensitivity in a climate model. *Climate Dyn.*, **19**, 211-236.
- Rahmstorf, S., 1993: A fast and complete convection scheme for ocean models. *Ocean Modell.*, **101**, 9-11.
- Randel, W. J., and F. Wu, 1999: A stratospheric ozone trends data set for global modelling studies. *Geophys. Res. Lett.*, **26**, 3089-3092.
- Risien, C. M., and D. B. Chelton, 2008: A global climatology of surface wind and wind stress fields from 8 years of QuikSCAT scatterometer data. *Submitted to Journal of Physical Oceanography*.
- Ringer, M. A., G. M. Martin, C. Z. Greeves, T. J. Hinton, P. M. James, V. D. Pope, A. A. Scaife, R. A. Stratton, P. M. Inness, J. M. Slingo, and G.-Y. Yang, 2006: The Physical Properties of the Atmosphere in the New Hadley Centre Global Environmental Model (HadGEM1). Part II: Aspects of Variability and Regional Climate. *J. Climate*, **19**, 1302-1326.
- Roberts, M. J., H. Banks, N. Gedney, J. Gregory, R. Hill, S. Mullerworth, A. Pardaens, G. Rickard, R. Thorpe, and R. Wood, 2004: Impact of an eddy-permitting ocean resolution on control and climate change simulations with a global coupled GCM, *J. Climate*, **17**, 3-20.
- Roberts, M. J. and D. Marshall, 1998: Do we require adiabatic dissipation schemes in eddy-resolving ocean models? *J. Phys. Oceanog.*, **28**, 2050-2063.
- Roberts, M. J., A. Clayton, M.-E. Demory, J. Donners, P. L. Vidale, W. A. Norton, L. C. Shaffrey, I. Stevens, R. A. Wood and J. Slingo, 2008a: UJCC: Impact of resolution on the tropical Pacific circulation in a matrix of coupled models, *Submitted to J. Climate*.
- Roberts, M. J. *et al.* 2008b: UJCC: ENSO mechanisms and feedbacks in a matrix of coupled models with different resolutions. *To be submitted to J. Climate*.

- Roberts, M. J., J. Donners, J. Harle, and I. Stevens, Impact of relative atmosphere-ocean resolution on coupled climate models, 2008c: *CLIVAR Exchanges*, **44**.
- Rundick, D. L., 1997: Direct velocity measurements in the Samoan Passage. *Journal of Geophysical Research*, **102**, 3293-3302.
- Russell, J.L. and Stouffer, R.J. and Dixon, K.W., 2006: Intercomparison of the Southern Ocean Circulations in IPCC Coupled Model Control Simulations. *J. Climate*, **19**, 4560-4575.
- Sakamoto, T.T., A. Sumi, S. Emori, T. Nishimura, H. Hasumi, T. Suzuki and M. Kimoto, 2004: Far-reaching effects of the Hawaiian Islands in the CCSR/NIES/FRCGC high-resolution climate model. *Geophys. Res. Letters*, **31**, L17212.
- Sardeshmukh, P.D. and Hoskins, B.J., 1988: On the generation of global rotational flow by steady idealised tropical divergence. *J. Atmos. Sci.*, **45**, 1228-1251.
- Semtner, A. J., 1976: A model for the thermodynamic growth of sea ice in numerical investigations of climate. *J. Phys. Oceanog.*, **6**, 379-389.
- Semtner, A. J. and R. M. Chervin, 1988: A Simulation of the Global Ocean Circulation With Resolved Eddies. *Journal of Geophysical Research*, **93**, 15502-15522.
- Semtner, A. J. and R. M. Chervin, 1992: Ocean General Circulation From a Global Eddy-Resolving Model. *Journal of Geophysical Research*, **97**, 5493-5550.
- Shaffrey, L.C. *et al.*, 2008: UK-HiGEM: The New UK High Resolution Global Environment Model. Weather and atmospheric variability. *To be submitted to J. Climate*.
- Slingo, J. M., P. M. Inness, R. B. Neale, S. J. Woolnough and G-Y. Yang, 2003: Scale interactions on diurnal to seasonal timescales and their relevance to model systematic errors. *Annales Geophysicae*, **46**, 139-155.
- Small, J., S.-P. Xie, and Y. Wang, 2003: Numerical simulation of the atmospheric response to Pacific tropical instability waves, *J. Climate*, **16**, 3722-3740.

- Smith, W. H. F. and D. Sandwell, 1997: Global seafloor topography from satellite altimetry and ship depth soundings. *Science*, **277**, 1956-1962.
- Smith, R.D., M. E. Maltrud, F. O. Bryan and M. W. Hect, 2000: Numerical Simulation of the North Atlantic Ocean at 1/10°. *Journal of Physical Oceanography*, **30**, 1532-1561.
- Smith, S. J., R. Andres, E. Conception, and J. Lurz, 2004: Historical sulfur dioxide emissions 1850-2000: Methods and results. PNNL Rep. 14537, Joint Global Change Research Institute, College Park, MD, 13pp.
- Spencer, H. and Slingo J.M., 2002: The Simulation of Peak and Delayed ENSO Teleconnections. *J. Climate*, **16**, 1757-1774.
- Spiro, P. A., D. J. Jacob, and J. A. Logan, 1992: Global inventory of sulfur emissions with 1° x 1° resolution. *J. Geophys. Res.*, **97**, 6023-6036.
- Stevens, D.P. *et al.* 2008: UK-HiGEM: The New UK High Resolution Global Environment Model. Ocean spin-up and evaluation. *To be submitted to Ocean Science*.
- Strachan, J., Understanding and modelling the climate of the maritime continent, *Ph.D. thesis*, University of Reading, PhD thesis, 2007.
- Sutton, R.T., W.A. Norton and S.P. Jewson, 2001: The North Atlantic Oscillation - What Role for the Ocean? *Atmospheric Science Letters*, **1**, 89-100.
- Taylor, C.M., D.J. Parker and P.P. Harris, 2007: An observational case study of mesoscale atmospheric circulations induced by soil moisture, *Geophys. Res. Letters*, **34**, doi:10.1029/2007GL030572.
- Thompson, S. R., 1995: Sills of the global ocean: A compilation. *Ocean Modell.*, **109**, 7-9.
- Timmermann R., P. Lemke, and C. Kottmeier, 1999: Formation and maintenance of a polynya in the Weddell Sea, *J. Phys. Oceanogr*, **29**, 1251-1264.
- Trenberth, K.E. and J.M. Caron, 2001: Estimates of Meridional Atmosphere and Ocean Heat Transports, *J. Climate*, **14**, 3433-3443.

- Trenberth, K. E., L. Smith, T. Qian, A. Dai and J. Fasullo, 2007: Estimates of the Global Water Budget and Its Annual Cycle Using Observational and Model Data. *J. Hydrometeorol.*, **8**, 758-769.
- Visbeck, M., J. Marshall, T. Haine and M. Spall, 1997: Specification of eddy transfer coefficients in coarse-resolution ocean circulation models. *J. Phys. Oceanog.* **27**, 381-402.
- Wajsowicz, R. C., 2002: A Modified Sverdrup Model of the Atlantic and Caribbean Circulation, *Journal of Physical Oceanography*, **32**, 973-993.
- Wallace, J. M., T. P. Mitchell and C. Deser, 1989: The influence of sea surface temperature on surface wind in the eastern equatorial Pacific: Seasonal and interannual variability, *J. Climate*, **2**, 1492-1499.
- Webster S., Brown A.R., Cameron D.R. and Jones C.P., 2003. Improvements to the representation of orography in the Met Office Unified Model., *Quart. J. Royal Meteorol. Soc.*, **129**, 1989-2010.
- Woodage, M. J., A. Slingo, S. Woodward, and R. Comer, 2008: UK-HiGEM: Simulations of desert dust and biomass burning aerosols with a high resolution atmospheric GCM. *To be submitted to J. Climate*.
- Woodgate, R. A. and Aagaard, K. and Weingartner, T., 2005: Monthly Temperature, Salinity and Transport Variability of the Bering Strait Throughflow, *Geophysical Research Letters*, **32**, doi:10.1029/2004GL021880.
- Wild, M. and E. Roeckner, 2006: Radiative fluxes in the ECHAM5 general circulation model. *J. Climate*, **19**, 3792-3809.
- Xie, P. and P. Arkin, 1997: Global Precipitation: A 17-year monthly analysis based on gauge observations, satellite estimates, and numerical model outputs, *Bulletin of the American Meteorological Society*, **78**, 2539-2558.

## Table Captions

Table 1: Annual global means of radiation and energy budget quantities from observational estimates, HiGEM1.2 and HadGEM1.2 control runs. The observed estimates are taken from Kiehl and Trenberth (1997) and Wild and Roeckner (2006), adjusted to produce consistency between the various components. Uncertainties in the top of the atmosphere fluxes are  $\pm 5\text{Wm}^{-2}$ . There are larger uncertainties at the surface. For example, estimates of the net surface solar radiation vary from 142 to  $168\text{Wm}^{-2}$ . Observed values of precipitation and P-E are from Trenberth *et al.* (2007). Unless otherwise stated, all values are in  $\text{Wm}^{-2}$ .

Table 2: Global annual mean loadings of aerosol in HiGEM1.2 and HadGEM1.2

## Figure Captions

Figure 1: Timeseries of global annual means for HiGEM1.2 (solid line) and HadGEM1.2 (dashed line) of a) absorbed solar radiation ( $\text{Wm}^{-2}$ ), b) net surface solar radiation ( $\text{Wm}^{-2}$ ), c) global mean surface temperature (K), d) TOA outgoing thermal radiation ( $\text{Wm}^{-2}$ ), e) net TOA radiation ( $\text{Wm}^{-2}$ ) and f) global sea ice area ( $10^{12}\text{m}^2$ ).

Figure 2: Annual mean radiation budget at the top of the atmosphere from HiGEM1.2 (left) and the differences from the HadGEM1.2 (right) for a) reflected solar radiation, b) outgoing thermal radiation and c) net downward radiation. The contour intervals have been matched to those in Figure 13 of Martin *et al.* (2006), which also shows the ERBE observations. All units are  $\text{Wm}^{-2}$ .

Figure 3: 21 to 70 year annual mean HiGEM1.2 minus Levitus errors for a) SST and b) SSS. c) and d) the same but for HadGEM1.2 minus Levitus. HiGEM1.2 minus HadGEM1.2 differences for e) SST and f) SSS. Units K and PSU.

Figure 4: Annual mean 1.5m temperature errors a) HiGEM1.2 minus 1961-1990 CRU 1.5m temperature dataset b) HadGEM1.2 minus CRU 1.5m temperatures. Units K.

Figure 5: 21 to 70 year annual mean precipitation from a) the TRMM 3B43 10 year climatology (Huffman *et al.* 2007) and b) HiGEM1.2. Units  $\text{mm day}^{-1}$ .

Figure 6: 21 to 70 year annual mean precipitation errors. a) HiGEM1.2 minus CMAP b) HadGEM1.2 minus CMAP. Units  $\text{mm day}^{-1}$ .

Figure 7: 21 to 70 year DJF mean sea level pressure a) HiGEM1.2 minus ERA-40 b) HadGEM1.2 minus ERA-40. Units hPa.

Figure 8: 21 to 70 year DJF 200hPa zonal winds for a) ERA-40 and wind differences for b) HiGEM1.2 minus ERA-40 and c) HadGEM1.2 minus ERA-40. Units  $\text{ms}^{-1}$ .

Figure 9: a) HiGEM1.2 minus HadGEM1.2 DJF 500mb geopotential height difference. The contour interval is 20m. b) HiGEM1.2 minus HadGEM1.2 DJF precipitation difference (colours) and 200hPa divergence (contours) difference for years 21 to 70. The contour intervals are  $1\text{mm day}^{-1}$  and  $10^{-6}\text{s}^{-1}$ . For divergence red contours are positive and blue contours negative and the zero contour is not shown.

Figure 10: 21 to 70 year JJA 850hPa wind vector and windspeed differences for a) HiGEM1.2 minus ERA-40 and b) HadGEM1.2 minus ERA-40. Units  $\text{ms}^{-1}$ .

Figure 11: Annual mean vertically integrated loadings ( $\text{mg m}^{-2}$ ) from HiGEM1.2 (left) and the differences from HadGEM1.2 (right) of a) sulphate and b) biomass burning while c) shows the corresponding cloud droplet effective radii (microns).

Figure 12: Mean transports through critical sections of the worlds oceans for HadGEM1.2 and HiGEM1.2. Observational values were obtained Gordon (Indonesian Through Flow: 2001), Hansen and Osterhus (Iceland-Scotland: 2000), Baringer and Larsen (Florida Strait: 2001) , Fahrbach *et al.* (Fram Strait: 2001), Rundick (Samoa Passage: 1997), Cunningham *et al.* (Drake Passage: 2003), Macrander *et al.* (2005) and Jonsson and Briem (Denmark Strait: 2003), Woodgate *et al.*

(Bering Strait: 2005). Note the scaling on the x-axis is not linear.

Figure 13: Meridional Overturning Circulation from the Atlantic Ocean (contours) and Potential Temperature difference from WOA 2001 in a) HiGEM1.2 and b) HadGEM1.2. Units Sv.

Figure 14: Sea surface height variability from a) TOPEX/Posidon b) HiGEM1.2 (Years 21 to 70) and c) HadGEM1.2 (Years 21 to 70). Units cm.

Figure 15: Northward heat transport in PW ( $1PW=10^{15}W$ ) for (a) the Atlantic Ocean and (b) the Global Ocean. In both panels the total HiGEM1.2 transport is the solid black line, the total HadGEM1.2 transport is the solid grey line, and the NCEP derived estimate of Trenberth and Caron (2001) is the dashed black line. Other components of the total transport are also shown. The error bars indicate the direct ocean estimates of Ganachaud and Wunsch (2003).

Figure 16: The distribution of Northern Hemisphere sea ice fraction in a) March and b) September from HiGEM1.2, observations (Comiso *et al.* 1999) and HadGEM1.2

Figure 17: The distribution of Southern Hemisphere sea ice fraction in a) March and b) September from HiGEM1.2, observations (Comiso *et al.* 1999) and HadGEM1.2

Figure 18: Instantaneous fields of surface windstress divergence (colours) and SST (contours) from a) HiGEM1.2 and b) HadGEM1.2.

Figure 19: The monthly (thin solid) and 12-month running mean (thick solid) timeseries of Nino3.4

SSTs from a) HiGEM1.2 and from b) HadGEM1.2. c) The normalised power spectrum of Nino3 SSTs from HiGEM1.1 (red), HadGEM1.1 (blue) and from the HadISST observations for the period 1870-2002 (solid black) and 1958-2002 (dashed black).

Figure 20: El Nino DJF composite anomalies for SST and precipitation from a) the HadISST SST dataset and b) the CMAP precipitation dataset and from c) and d) HiGEM1.2 and e) and f) HadGEM1.2. Units K and  $\text{mm day}^{-1}$ .

Figure 21: El Nino DJF composite anomalies for mean sea level pressure from a) ERA-40 b) HiGEM1.2 and c) HadGEM1.2. Units hPa.

Figure 22: Annual mean windstress curl (colours) and SSTs (contours) from a) QuikSCAT windstresses (from Risien and Chelton 2008) and  $0.25^\circ$  WOA 2001 SSTs (Conkright *et al.* 2002), b) 21 to 70 year mean of HiGEM1.2 and c) 21 to 70 years mean of HadGEM1.2. Units  $\text{Nm}^{-2}$  per  $10^4\text{km}$  and K.

Parameter	Observed	HiGEM1.2	HadGEM1.2
Incoming Solar (TOA)	342	341.39	341.39
Outgoing Solar (TOA)	107	97.06	99.81
Absorbed Solar (TOA)	235	244.33	241.57
Outgoing Thermal (TOA)	235	243.66	241.33
Net Radiation (TOA)	0	0.67	0.25
Solar cloud radiative forcing (TOA)	-48	-43.37	-44.91
Thermal cloud radiative forcing	25	23.67	23.99
Net solar (Surface)	154	172.20	169.91
Net thermal (Surface)	-50	-61.93	-61.75
Net radiation (Surface)	104	110.27	108.16
Sensible heat flux	25	18.74	18.49
Latent heat flux	79	89.89	88.36
Precipitation (mm day <sup>-1</sup> )	2.60	3.11	3.05
P-E over Land (mm day <sup>-1</sup> )	0.73	0.72	0.70
P-E over Ocean (mm day <sup>-1</sup> )	-0.30	-0.30	-0.28
Cloud Cover (%)	60	52	53

Table 1: Annual global means of radiation and energy budget quantities from observational estimates, HiGEM1.2 and HadGEM1.2 control runs. The observed estimates are taken from Kiehl and Trenberth (1997) and Wild and Roeckner (2006), adjusted to produce consistency between the various components. Uncertainties in the top of the atmosphere fluxes are  $\pm 5 \text{Wm}^{-2}$ . There are larger uncertainties at the surface. For example, estimates of the net surface solar radiation vary from 142 to 168  $\text{Wm}^{-2}$ . Observed values of precipitation and P-E are from Trenberth *et al.* (2007). Unless otherwise stated, all values are in  $\text{Wm}^{-2}$ .

Aerosol Type	HiGEM1.2	HadGEM1.2
S in Sulphate	0.52Tg	0.53Tg
Biomass	1.59Tg	1.51Tg
Black Carbon	0.30Tg	0.31Tg

Table 2: Global annual mean loadings of aerosol in HiGEM1.2 and HadGEM1.2

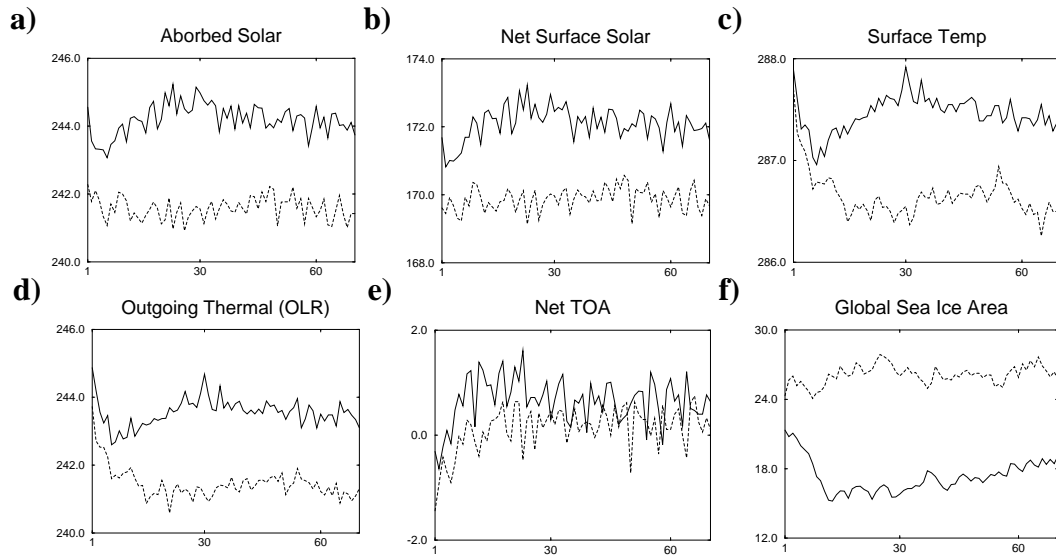


Figure 1: Timeseries of global annual means for HiGEM1.2 (solid line) and HadGEM1.2 (dashed line) of a) absorbed solar radiation ( $\text{Wm}^{-2}$ ), b) net surface solar radiation ( $\text{Wm}^{-2}$ ), c) global mean surface temperature (K), d) TOA outgoing thermal radiation ( $\text{Wm}^{-2}$ ), e) net TOA radiation ( $\text{Wm}^{-2}$ ) and f) global sea ice area ( $10^{12}\text{m}^2$ ).

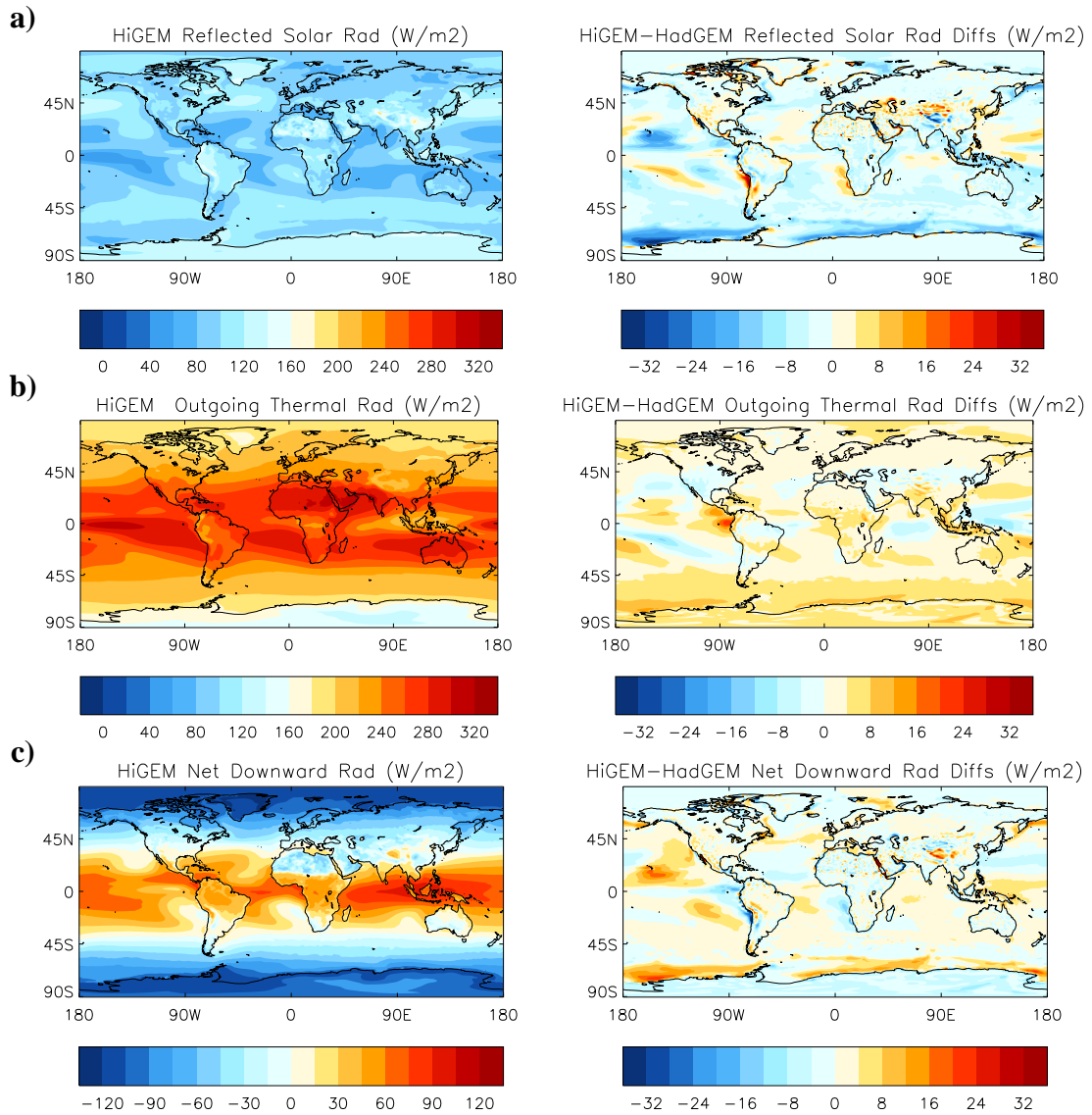


Figure 2: Annual mean radiation budget at the top of the atmosphere from HiGEM1.2 (left) and the differences from the HadGEM1.2 (right) for a) reflected solar radiation, b) outgoing thermal radiation and c) net downward radiation. The contour intervals have been matched to those in Figure 13 of Martin *et al.* (2006), which also shows the ERBE observations. All units are  $\text{Wm}^{-2}$ .

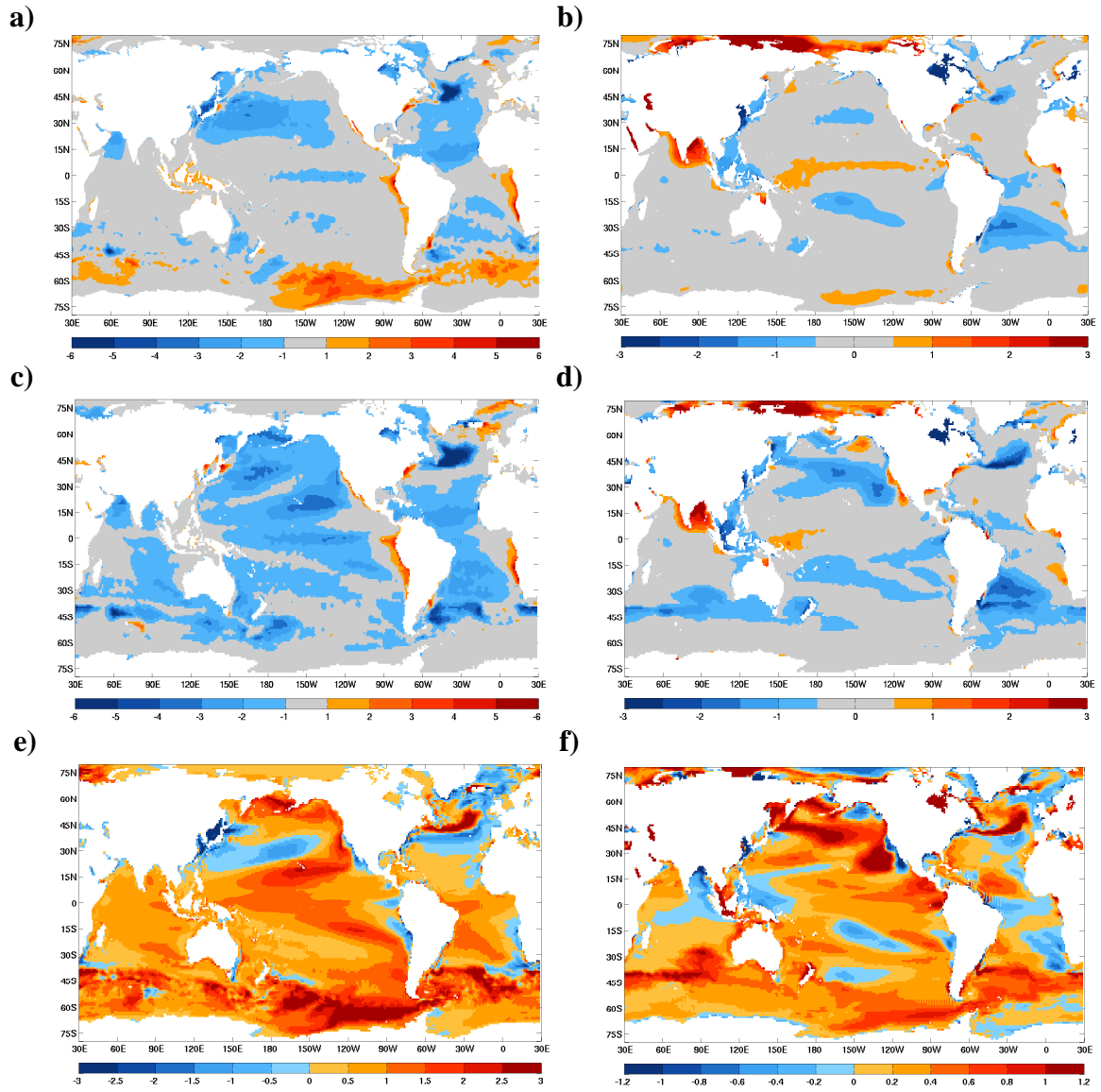


Figure 3: 21 to 70 year annual mean HiGEM1.2 minus Levitus errors for a) SST and b) SSS. c) and d) the same but for HadGEM1.2 minus Levitus. HiGEM1.2 minus HadGEM1.2 differences for e) SST and f) SSS. Units K and PSU.

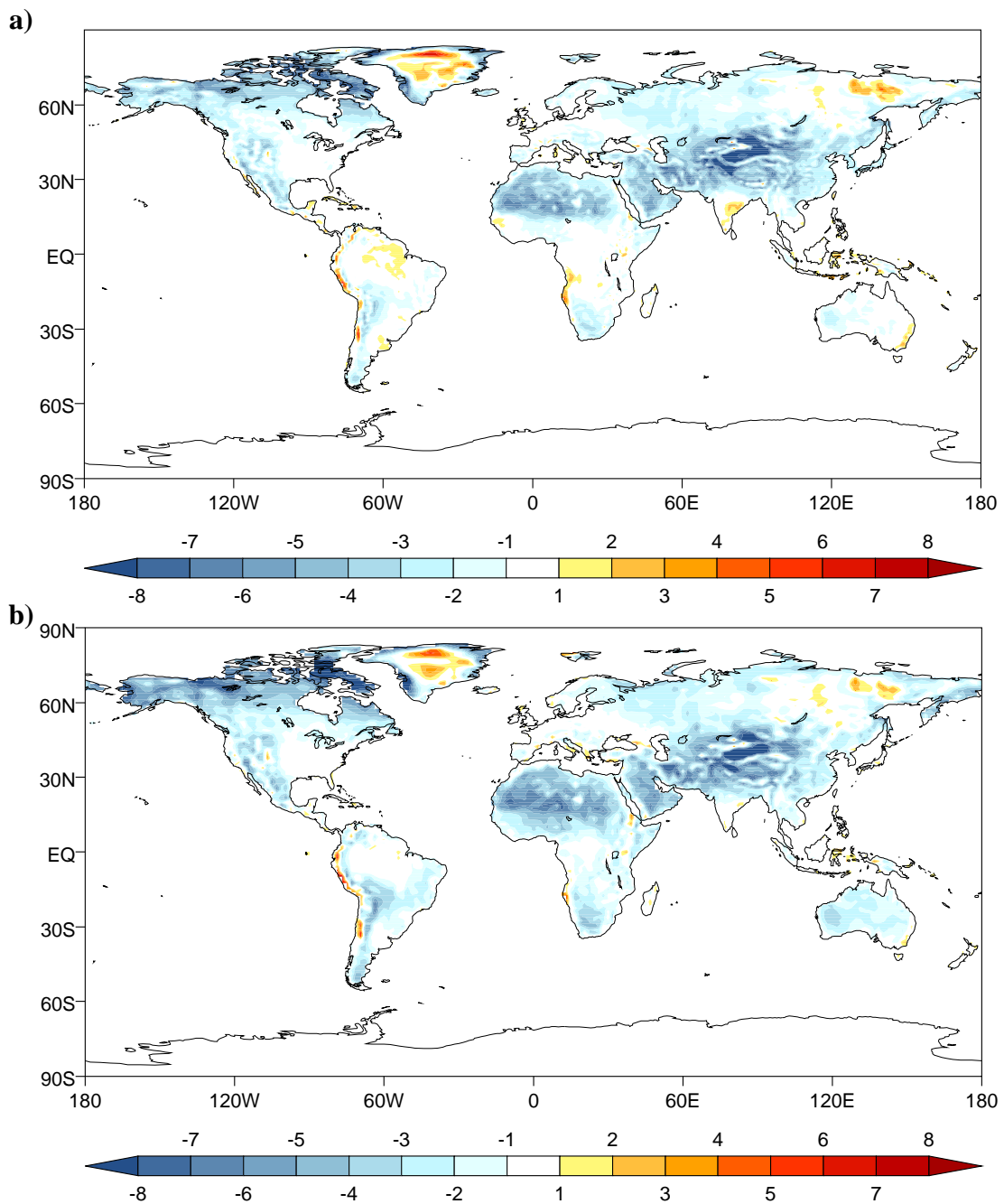


Figure 4: Annual mean 1.5m temperature errors a) HiGEM1.2 minus 1961-1990 CRU 1.5m temperature dataset b) HadGEM1.2 minus CRU 1.5m temperatures. Units K.

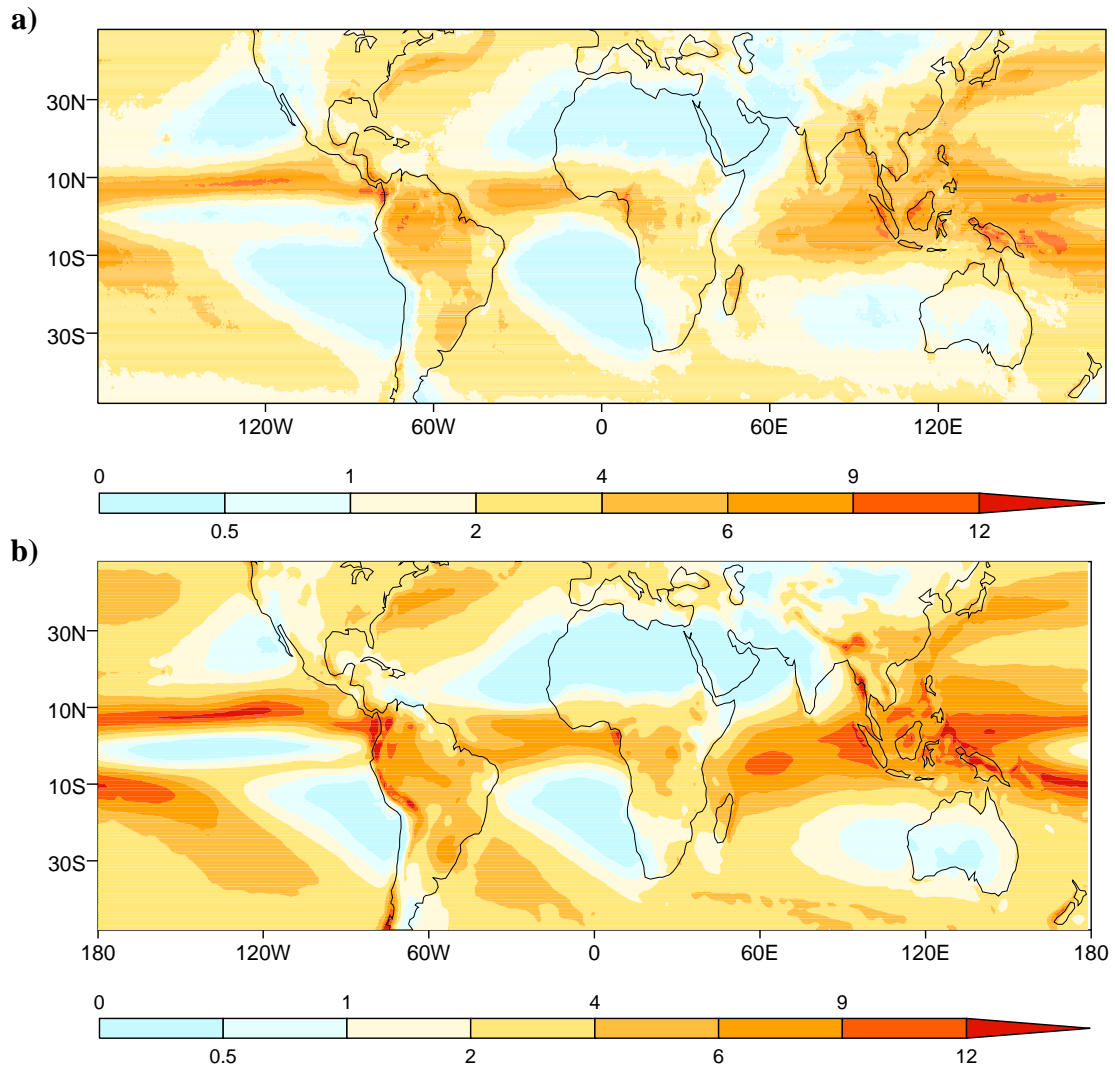


Figure 5: 21 to 70 year annual mean precipitation from a) the TRMM 3B43 10 year climatology (Huffman *et al.* 2007) and b) HiGEM1.2. Units  $\text{mm day}^{-1}$ .

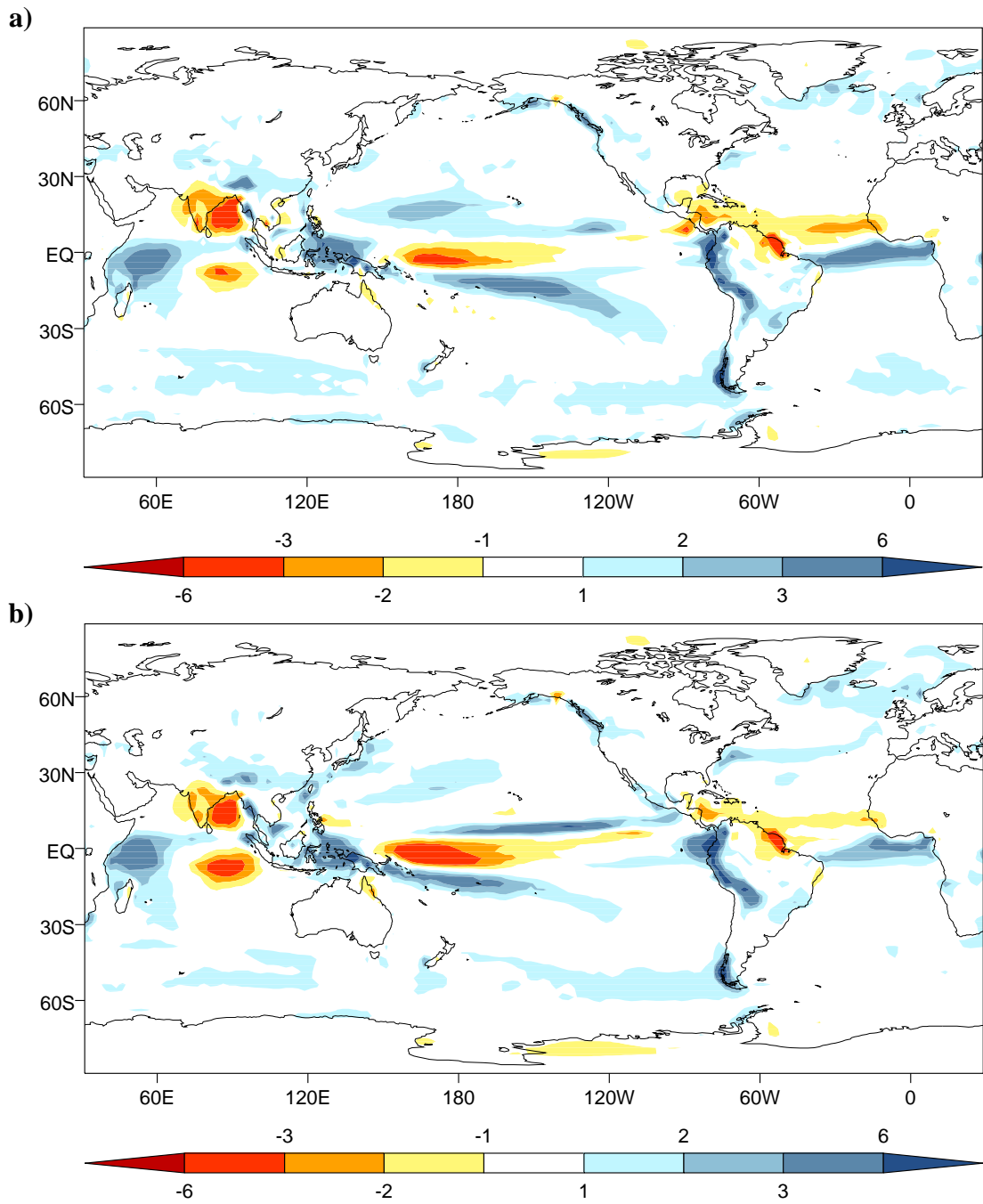


Figure 6: 21 to 70 year annual mean precipitation errors. a) HiGEM1.2 minus CMAP b) HadGEM1.2 minus CMAP. Units mm day<sup>-1</sup>.

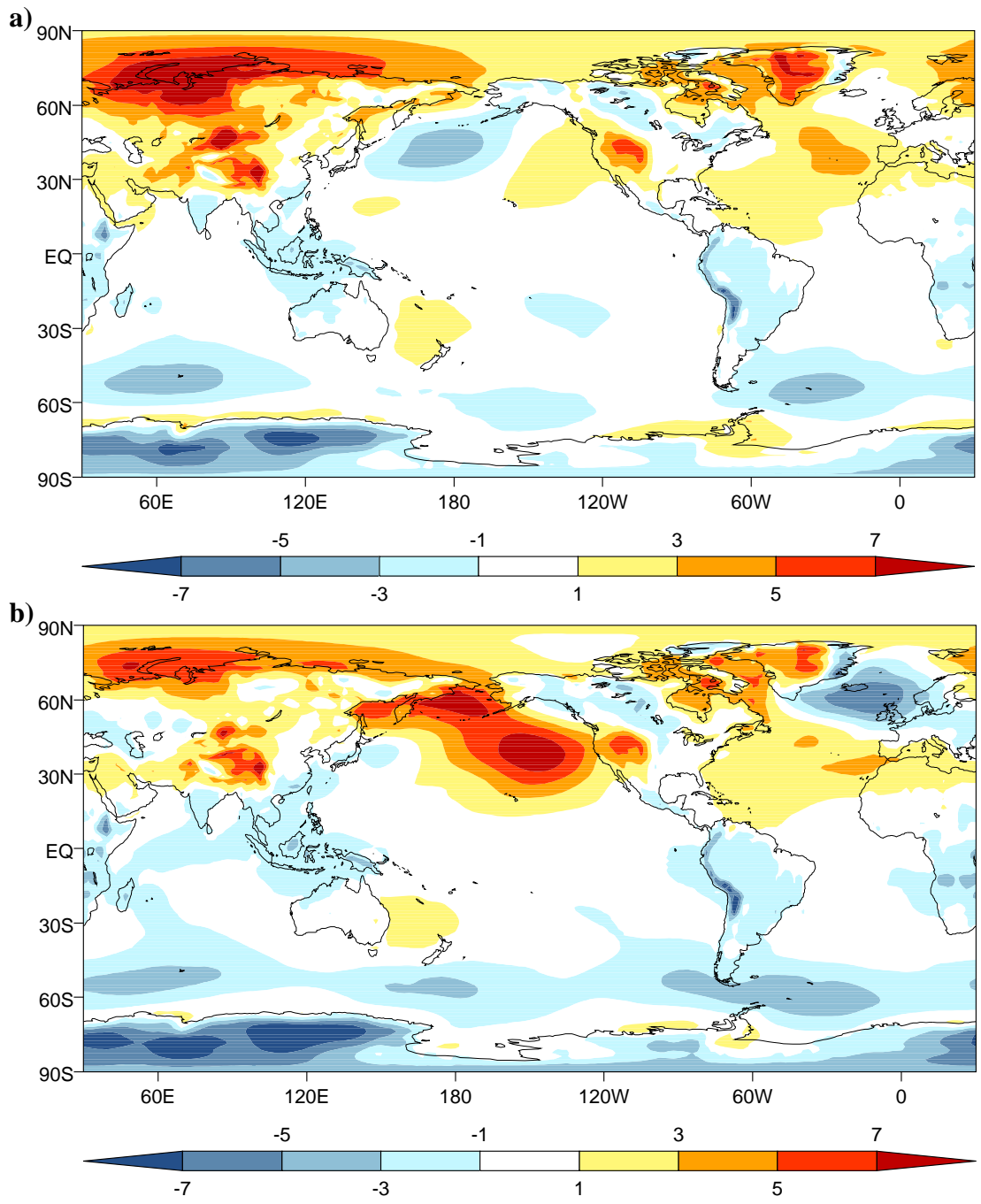


Figure 7: 21 to 70 year DJF mean sea level pressure a) HiGEM1.2 minus ERA-40 b) HadGEM1.2 minus ERA-40. Units hPa.

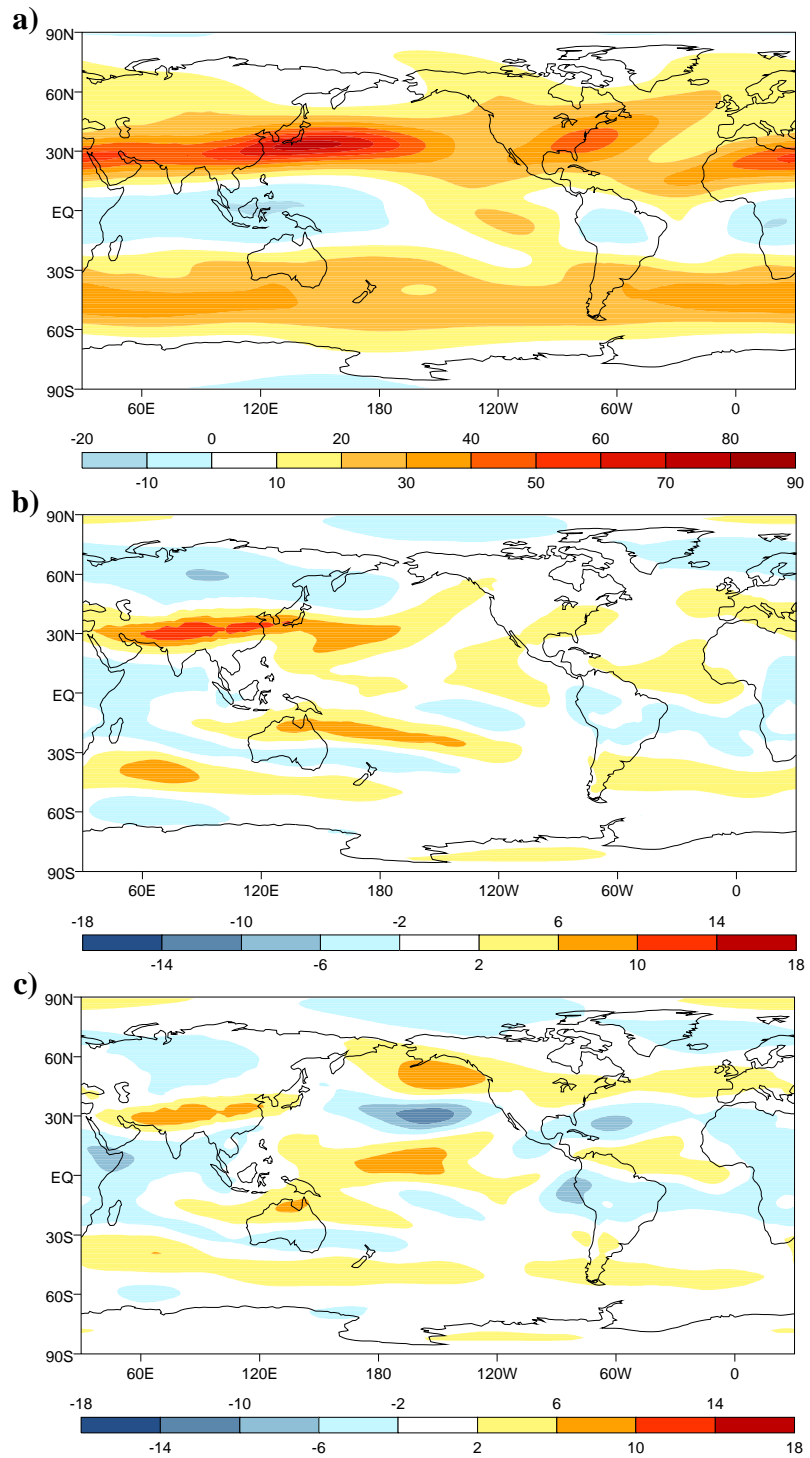


Figure 8: 21 to 70 year DJF 200hPa zonal winds for a) ERA-40 and wind differences for b) HiGEM1.2 minus ERA-40 and c) HadGEM1.2 minus ERA-40. Units ms<sup>-1</sup>.

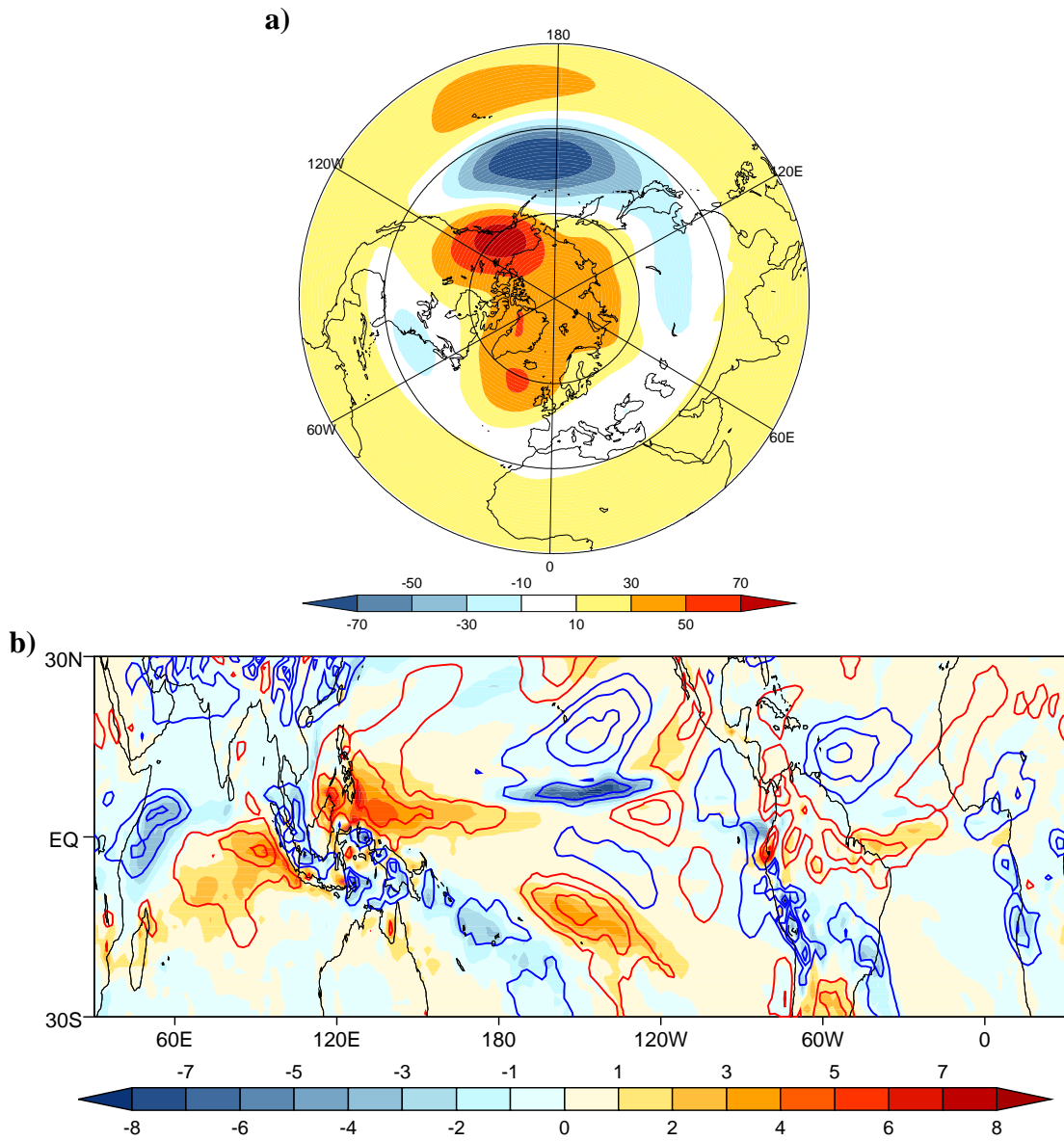


Figure 9: a) HiGEM1.2 minus HadGEM1.2 DJF 500mb geopotential height difference. The contour interval is 20m. b) HiGEM1.2 minus HadGEM1.2 DJF precipitation difference (colours) and 200hPa divergence (contours) difference for years 21 to 70. The contour intervals are 1mm day<sup>-1</sup> and 10<sup>-6</sup>s<sup>-1</sup>. For divergence red contours are positive and blue contours negative and the zero contour is not shown.

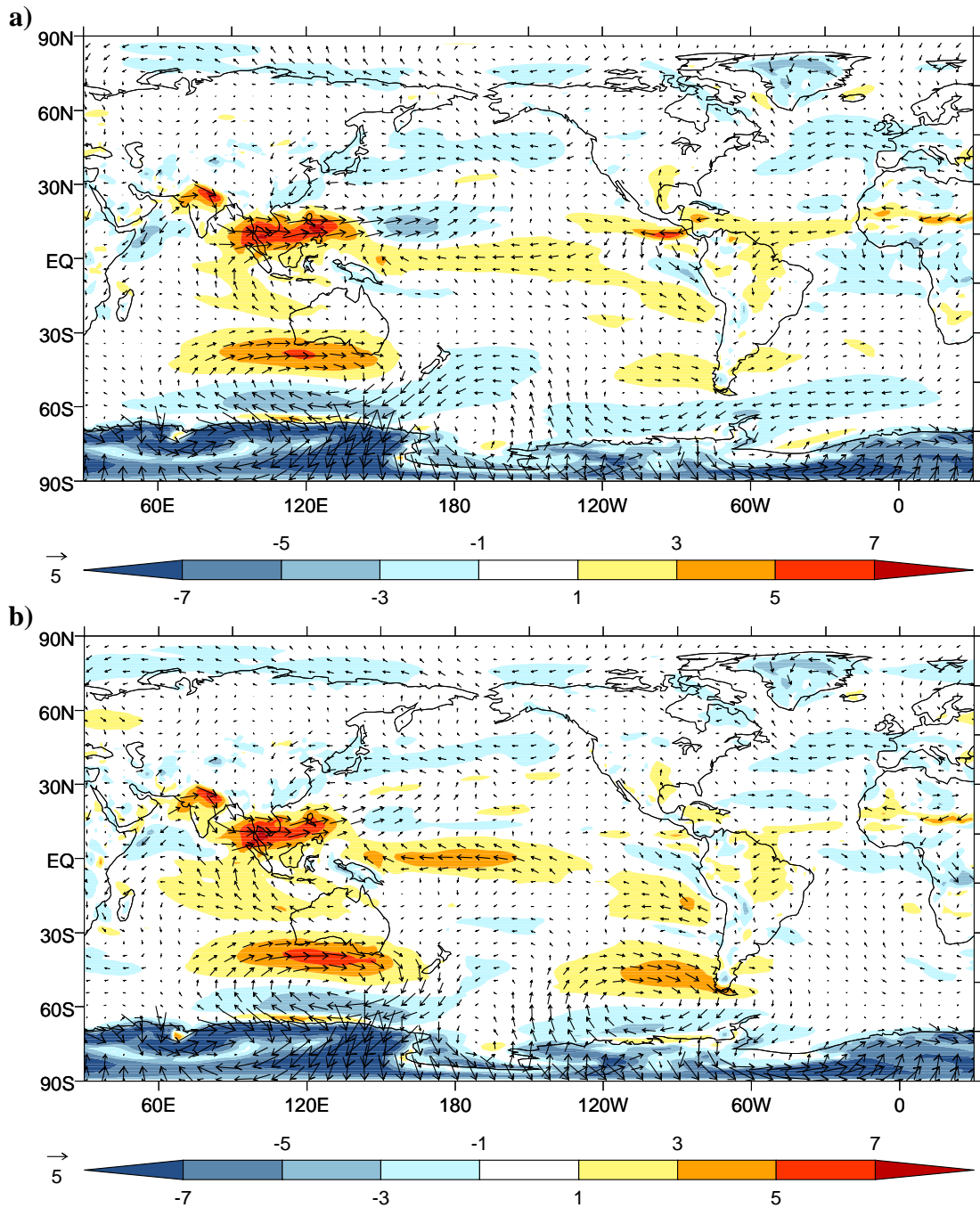


Figure 10: 21 to 70 year JJA 850hPa wind vector and windspeed differences for a) HiGEM1.2 minus ERA-40 and b) HadGEM1.2 minus ERA-40. Units  $\text{ms}^{-1}$ .

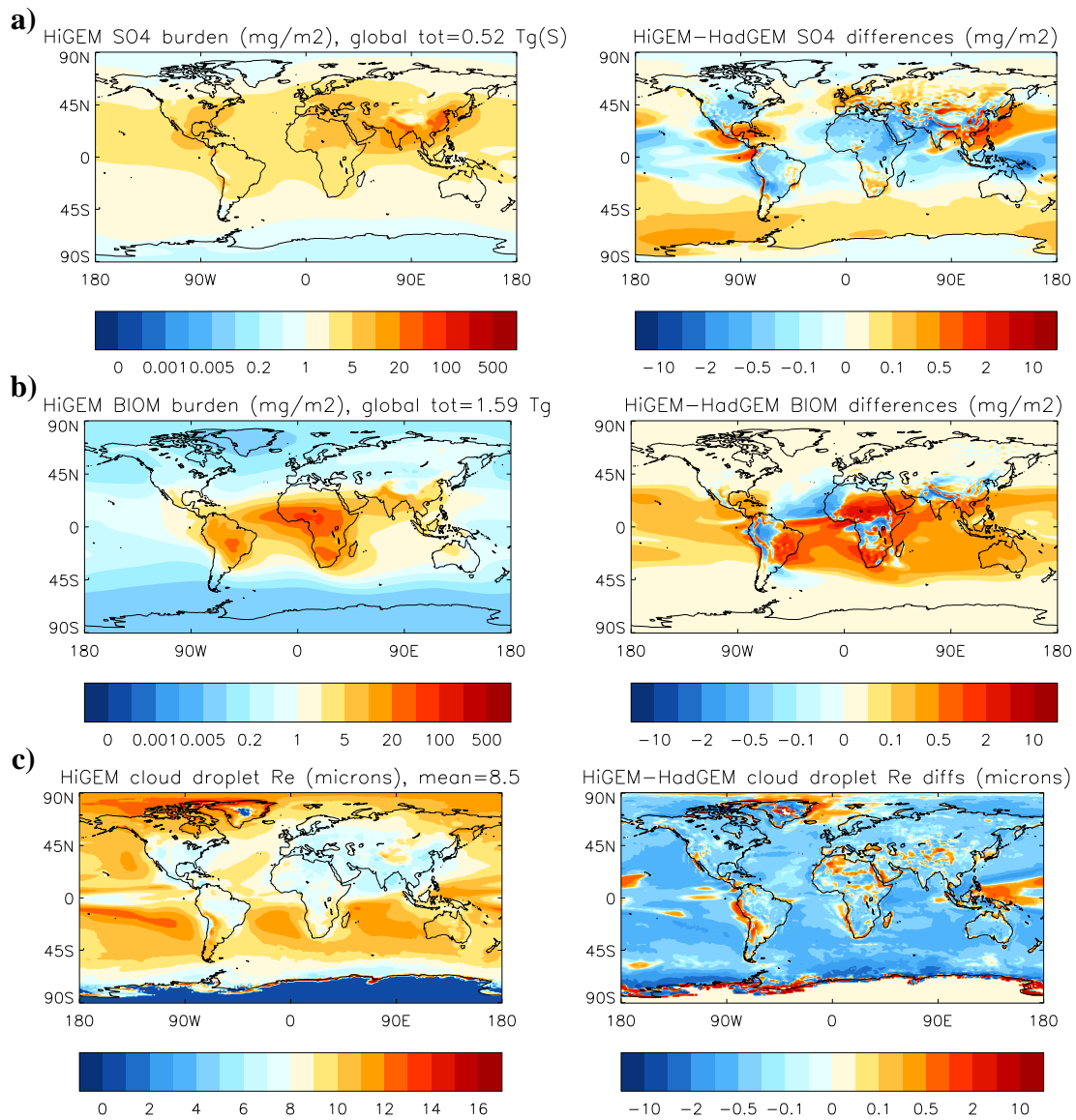


Figure 11: Annual mean vertically integrated loadings ( $\text{mg m}^{-2}$ ) from HiGEM1.2 (left) and the differences from HadGEM1.2 (right) of a) sulphate and b) biomass burning while c) shows the corresponding cloud droplet effective radii (microns).

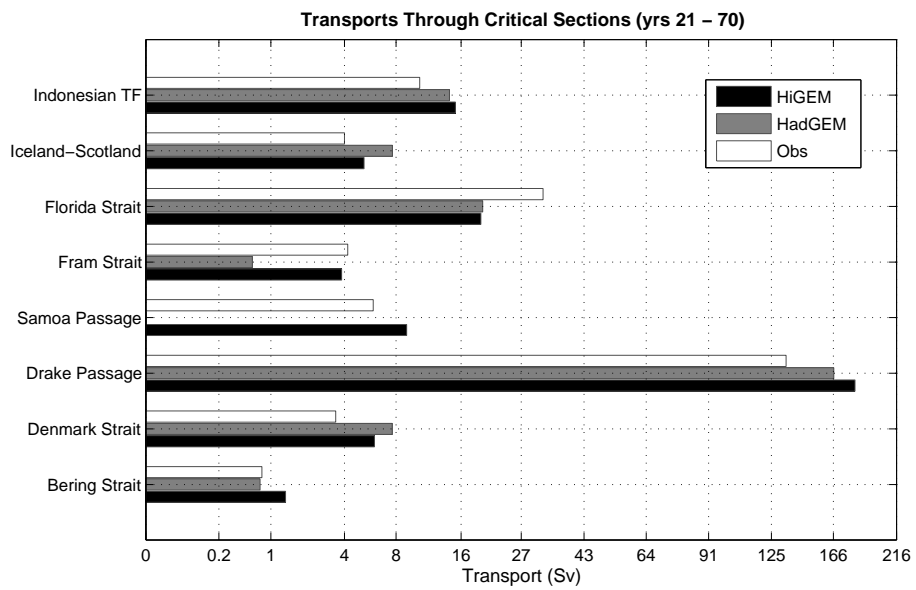


Figure 12: Mean transports through critical sections of the worlds oceans for HadGEM1.2 and HiGEM1.2. Observational values were obtained Gordon (Indonesian Through Flow: 2001), Hansen and Osterhus (Iceland-Scotland: 2000), Baringer and Larsen (Florida Strait: 2001) , Fahrbach *et al.* (Fram Strait: 2001), Rundick (Samoa Passage: 1997), Cunningham *et al.* (Drake Passage: 2003), Macrander at al (2005) and Jonsson and Briem (Denmark Strait: 2003), Woodgate *et al.* (Bering Strait: 2005). Note the scaling on the x-axis is not linear.

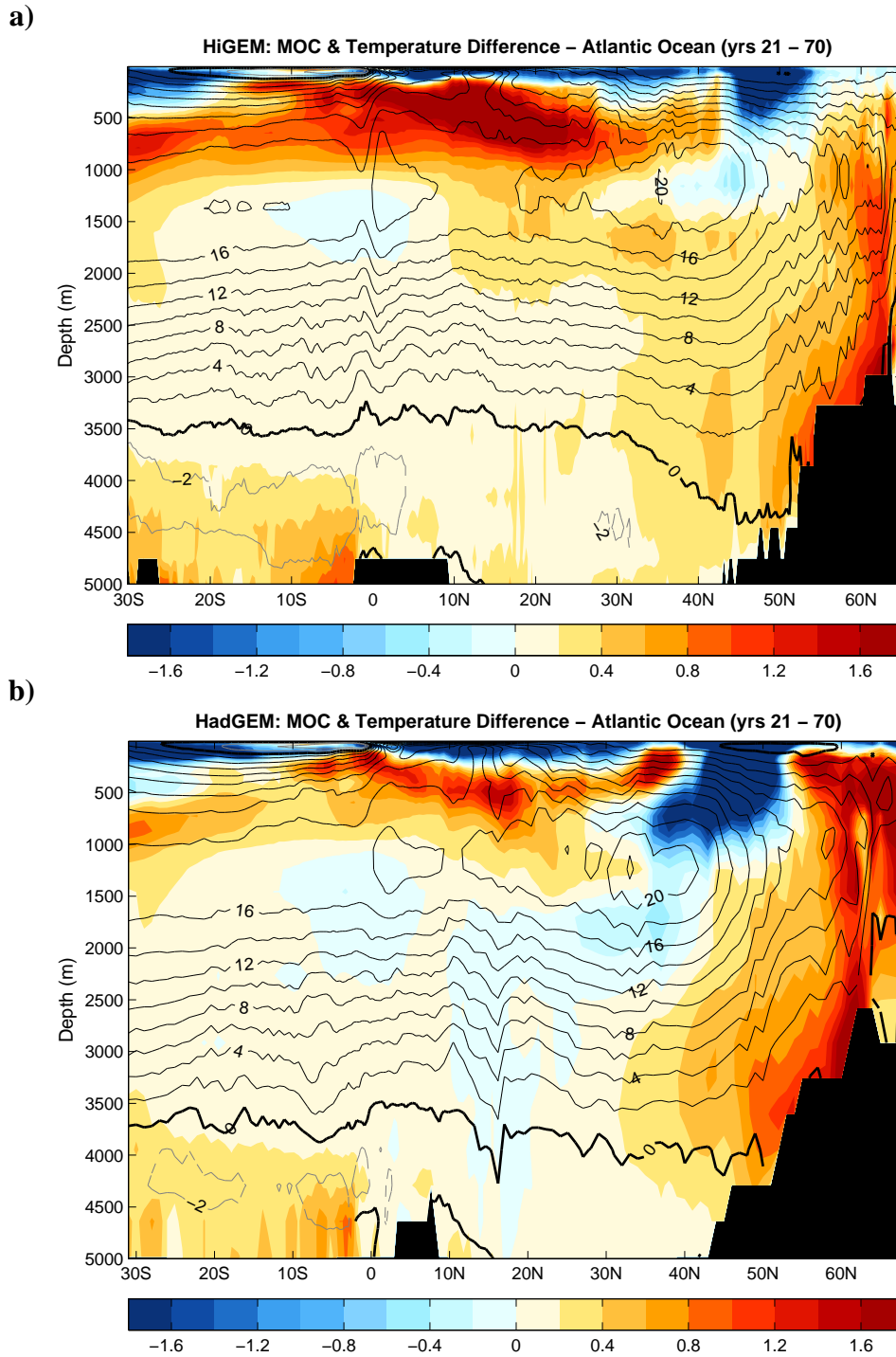


Figure 13: Meridional Overturning Circulation from the Atlantic Ocean (contours) and Potential Temperature difference from WOA 2001 in a) HiGEM1.2 and b) HadGEM1.2. Units Sv.

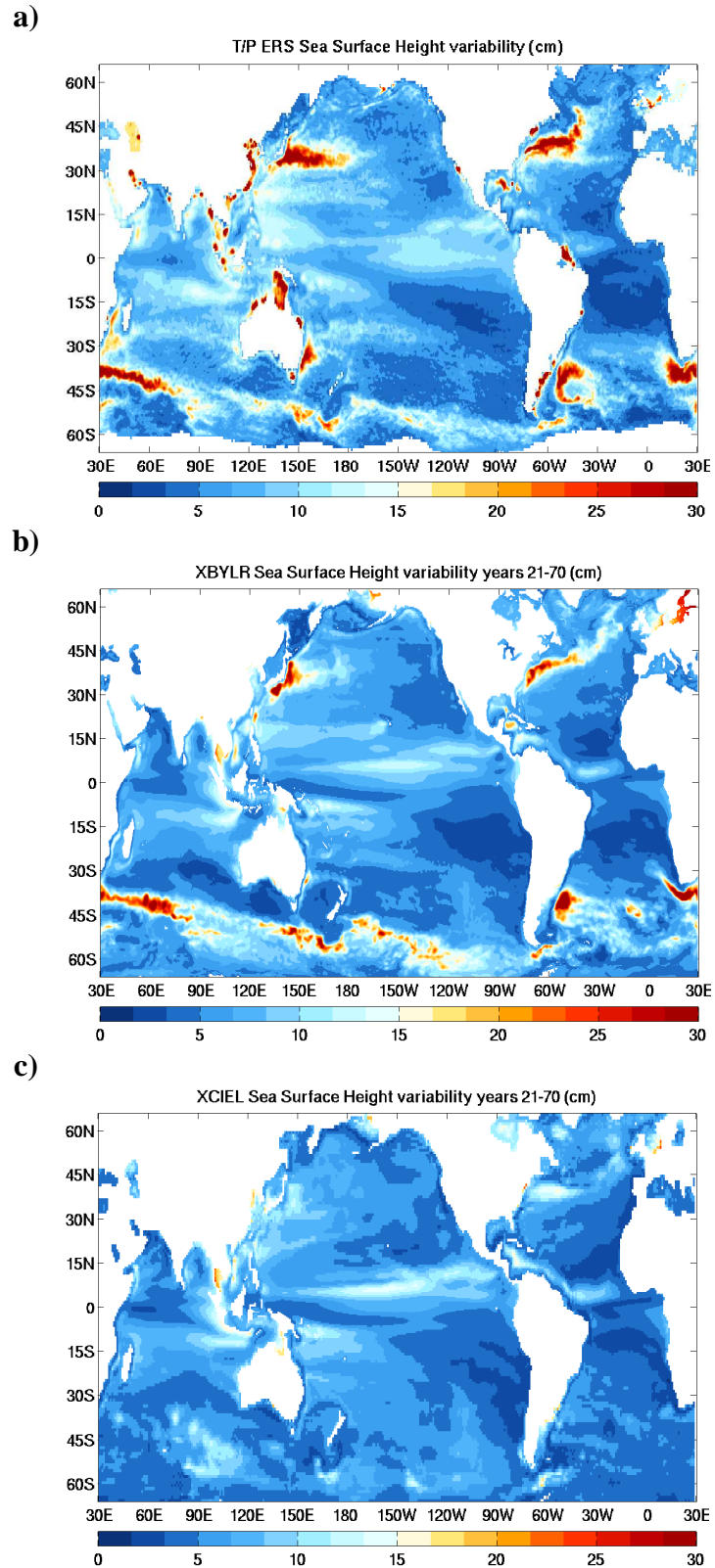


Figure 14: Sea surface height variability from a) TOPEX/Poseidon b) HiGEM1.2 (Years 21 to 70) and c) HadGEM1.2 (Years 21 to 70). Units cm.

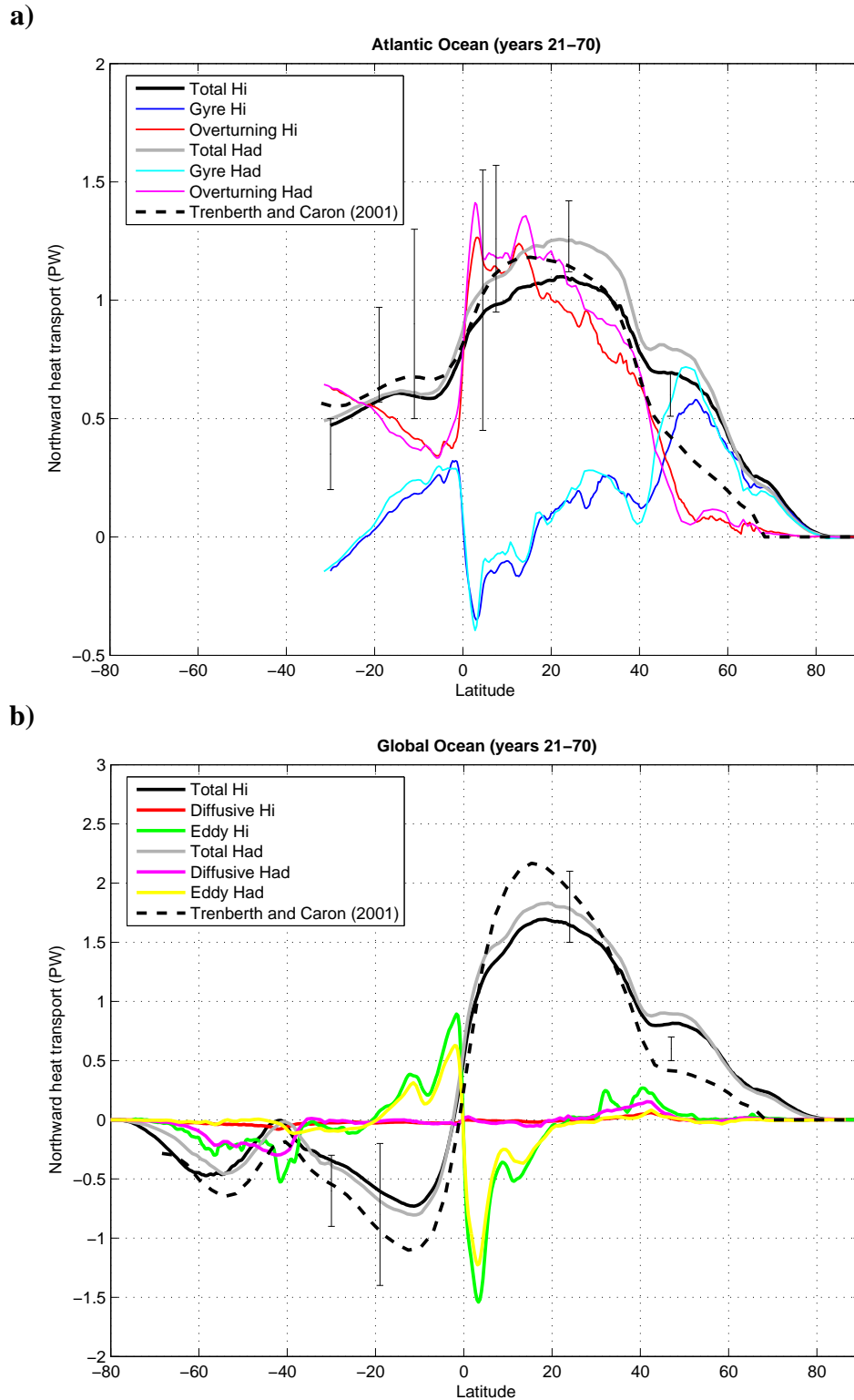


Figure 15: Northward heat transport in PW ( $1\text{PW}=10^{15}\text{W}$ ) for (a) the Atlantic Ocean and (b) the Global Ocean. In both panels the total HiGEM1.2 transport is the solid black line, the total HadGEM1.2 transport is the solid grey line, and the NCEP derived estimate of Trenberth and Caron (2001) is the dashed black line. Other components of the total transport are also shown. The error bars indicate the direct ocean estimates of Ganachaud and Wunsch (2003).

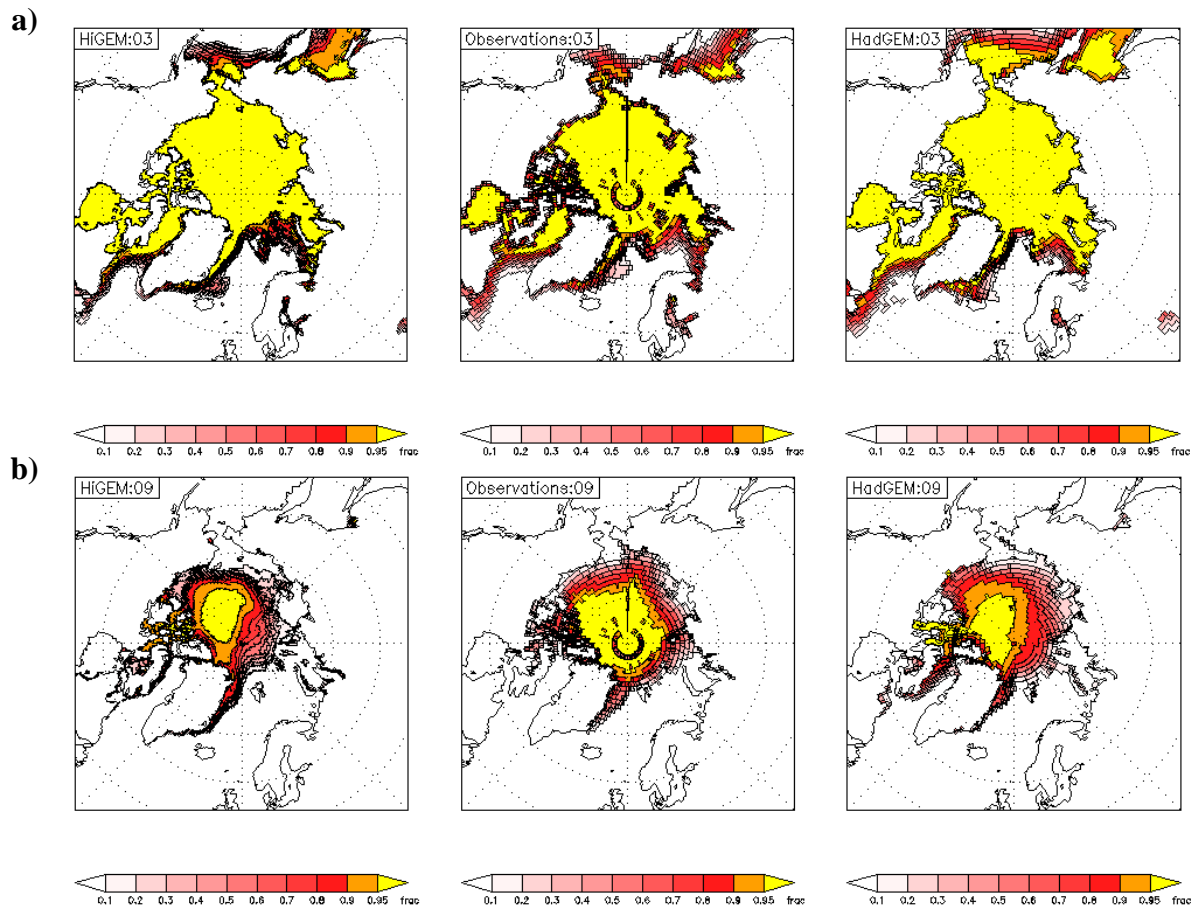


Figure 16: The distribution of Northern Hemisphere sea ice fraction in a) March and b) September from HiGEM1.2, observations (Comiso *et al.* 1999) and HadGEM1.2

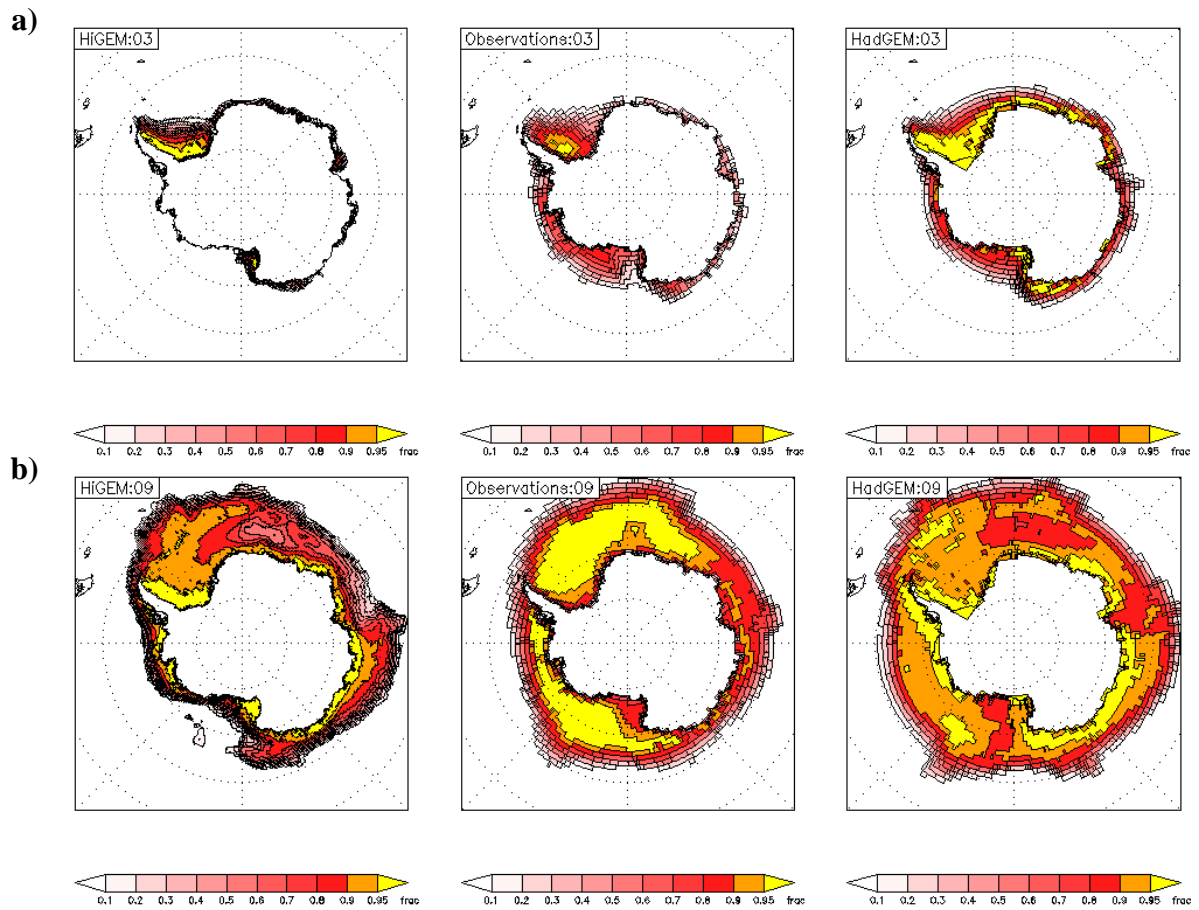


Figure 17: The distribution of Southern Hemisphere sea ice fraction in a) March and b) September from HiGEM1.2, observations (Comiso *et al.* 1999) and HadGEM1.2

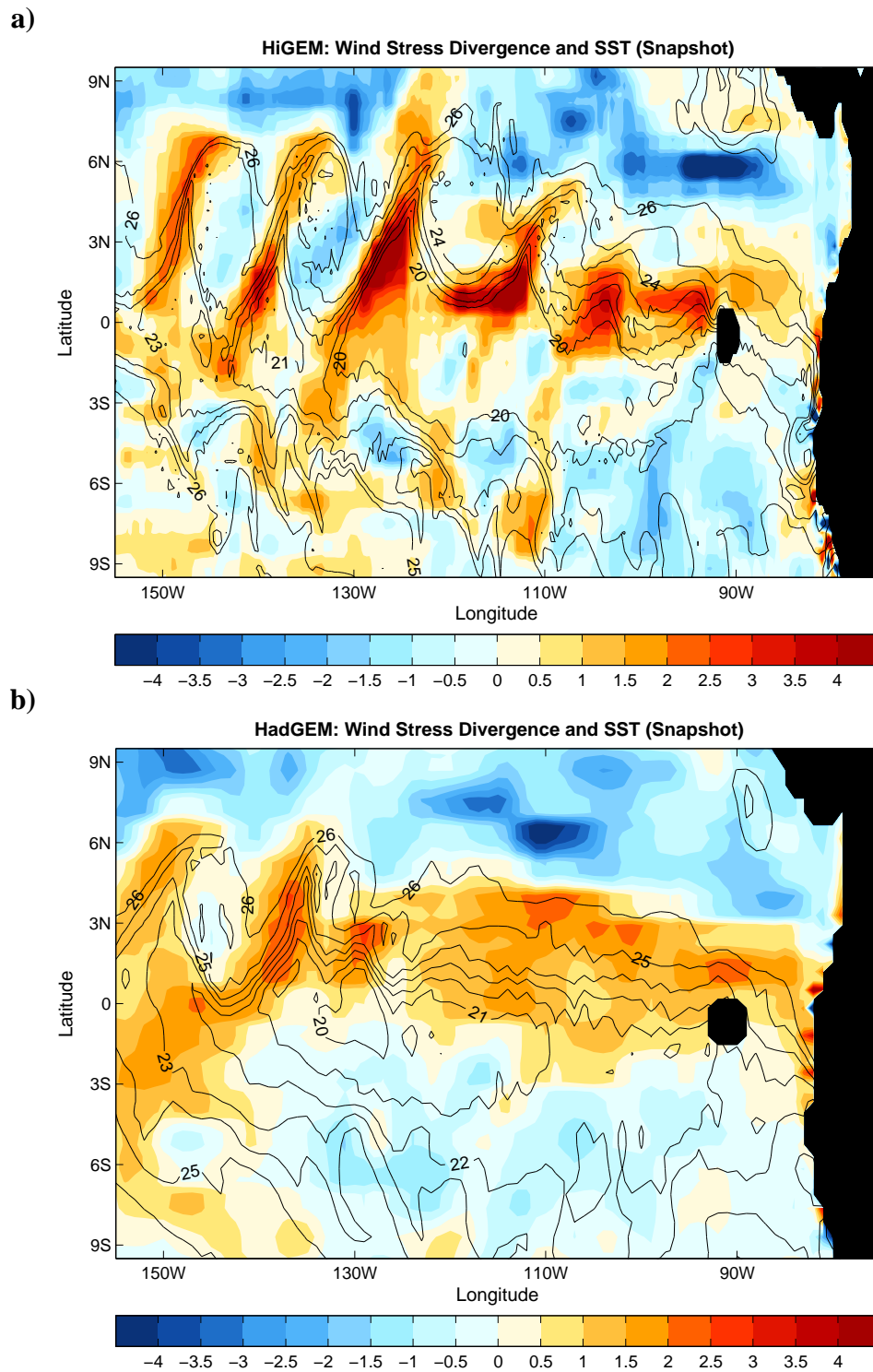


Figure 18: Instantaneous fields of surface windstress divergence (colours) and SST (contours) from a) HiGEM1.2 and b) and HadGEM1.2

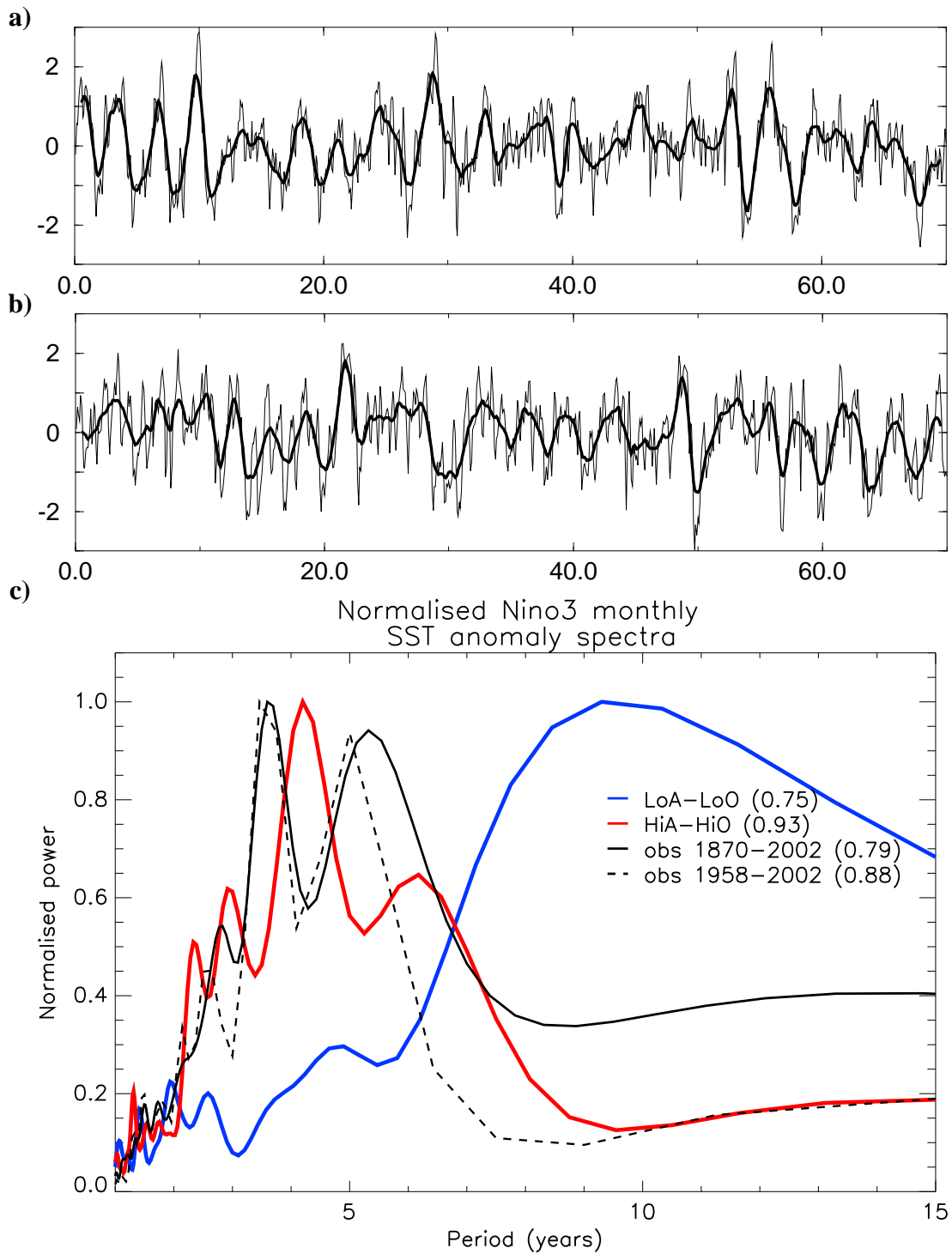


Figure 19: The monthly (thin solid) and 12-month running mean (thick solid) timeseries of Nino3.4 SSTs from a) HiGEM1.2 and from b) HadGEM1.2. c) The normalised power spectrum of Nino3 SSTs from HiGEM1.1 (red), HadGEM1.1 (blue) and from the HadISST observations for the period 1870-2002 (solid black) and 1958-2002 (dashed black).

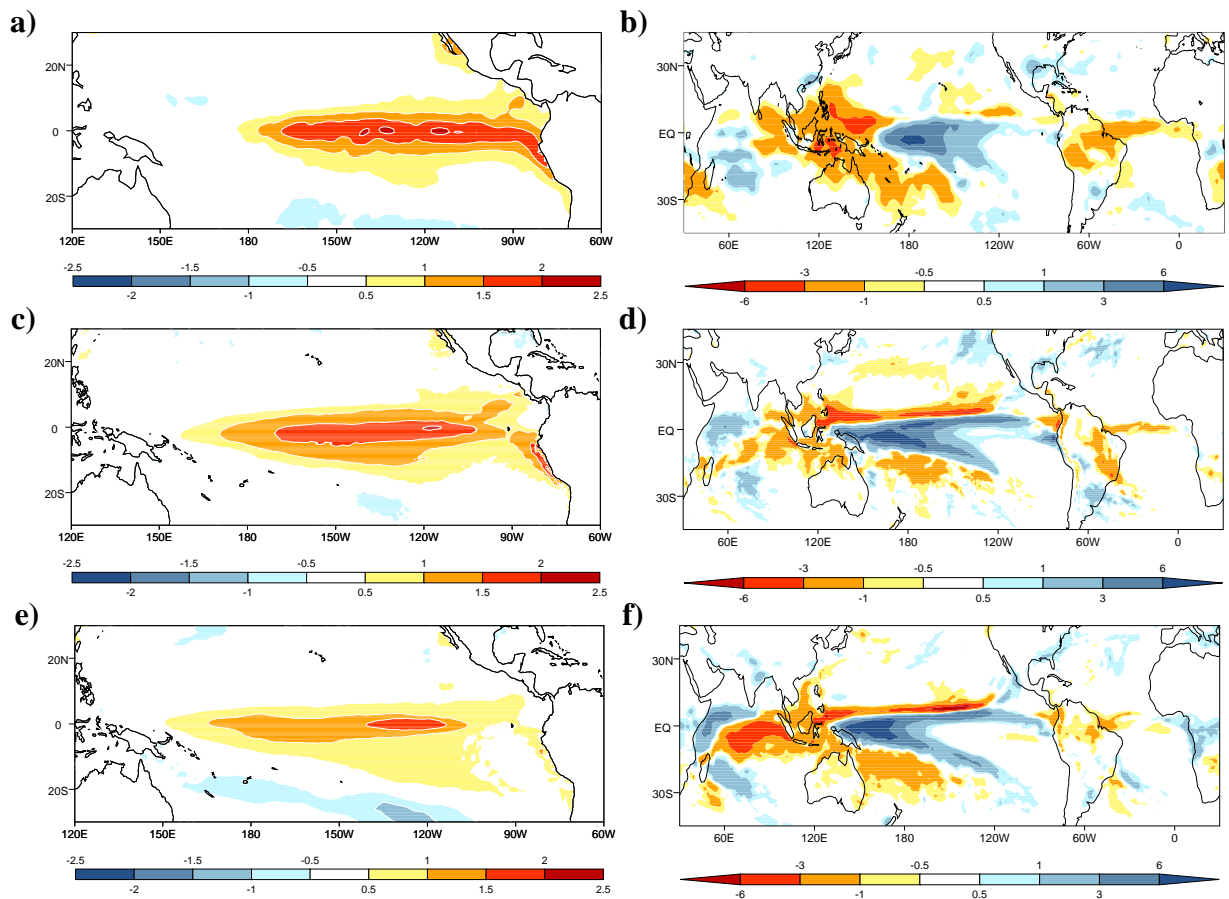


Figure 20: El Niño DJF composite anomalies for SST and precipitation from a) the HadISST SST dataset and b) the CMAP precipitation dataset and from c) and d) HiGEM1.2 and e) and f) HadGEM1.2. Units K and  $\text{mm day}^{-1}$ .

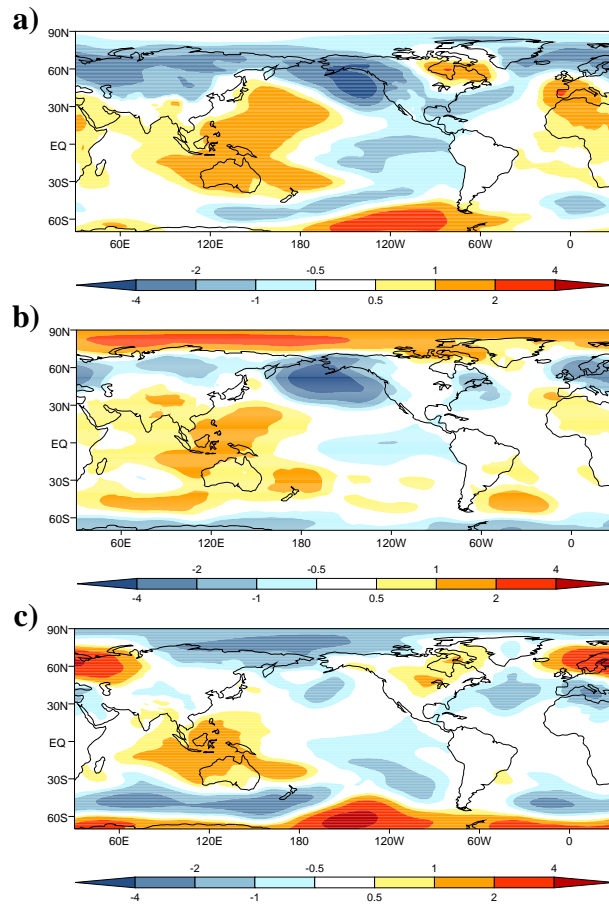


Figure 21: El Niño DJF composite anomalies for mean sea level pressure from a) ERA-40 b) HiGEM1.2 and c) HadGEM1.2. Units hPa.

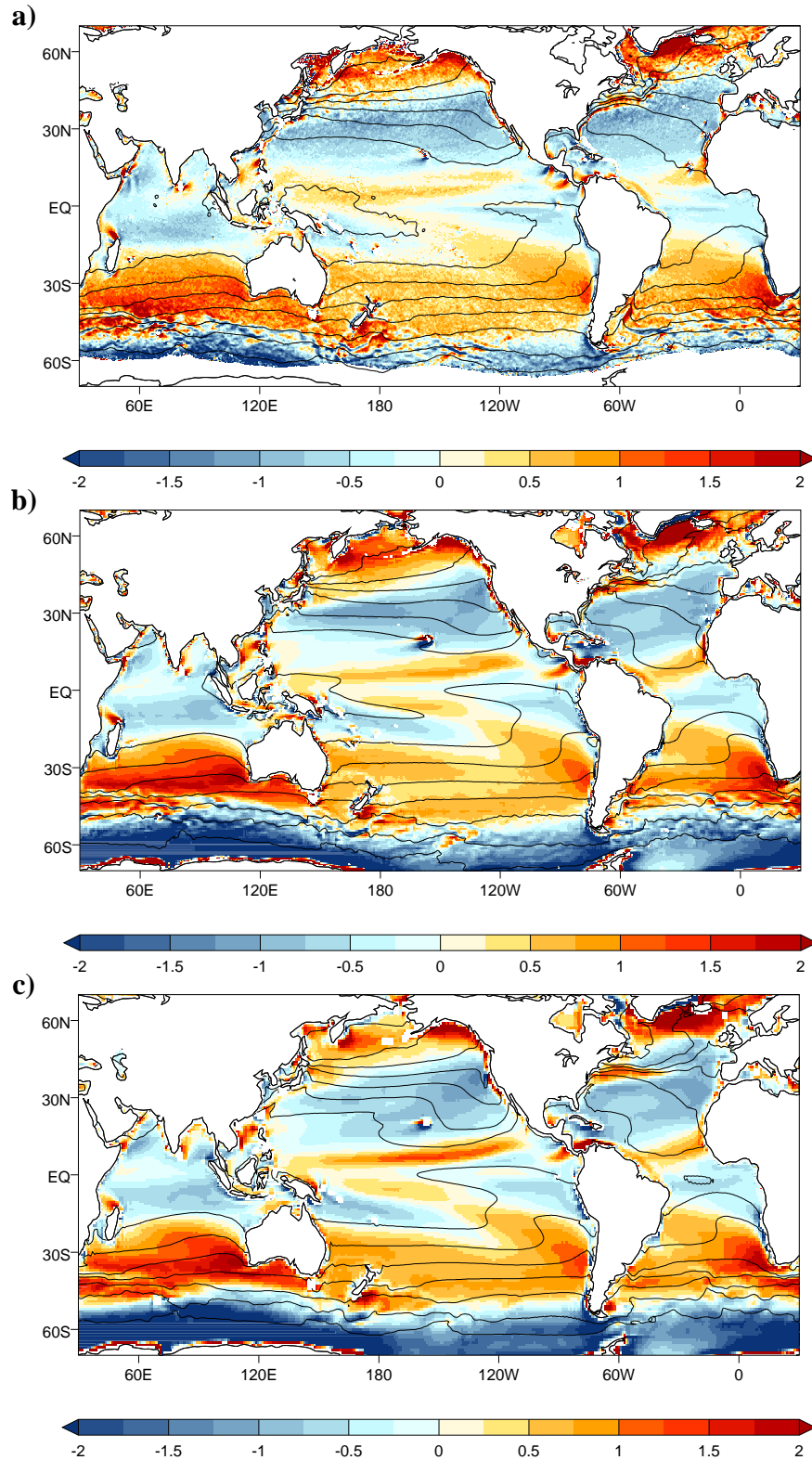


Figure 22: Annual mean windstress curl (colours) and SSTs (contours) from a) QuikSCAT windstresses (from Risien and Chelton 2008) and  $0.25^\circ$  WOA 2001 SSTs (Conkright *et al.* 2002), b) 21 to 70 year mean of HiGEM1.2 and c) 21 to 70 years mean of HadGEM1.2. Units  $\text{Nm}^{-2}$  per  $10^4\text{km}$  and K.